Advances in Aerodynamics

RESEARCH Open Access

Noise control for high subsonic jet flows by inner wall treatment

Huyue Mao[1], Xiaolong Tang[1*], Xiaoquan Yang[1], Jue Ding[1] and Peifen Weng[1,2]

*Correspondence:
tangxl@shu.edu.cn

[1] Shanghai Institute of Applied Mathematics and Mechanics, School of Mechanics and Engineering Science, Shanghai University, Shanghai 200444, China
[2] Shanghai University of Electric Power, Shanghai 200090, China

Abstract

Subsonic jet nozzles, commonly used in passenger aircrafts, generate significant noise that travels both downstream and upstream due to large-scale or fine-scale turbulence in the jet plume. To reduce jet noise, a novel wall treatment method, termed the wavy inner wall (WIW), is proposed. With this method, the smooth inner wall near the exit of the nozzle is replaced by treated walls that carry small wavy patterns. Numerical simulations were conducted to investigate the effects of the WIW treatment. Large eddy simulations (LES) were used to predict the unsteady flow field and the far-field noise, followed by the analogy method proposed by Ffowcs Williams and Hawkings. To better understand the mechanism behind the noise reduction achieved by the WIW treatment, the shear-layer instability, radial and azimuthal auto-correlation functions, turbulent kinetic energy, and acoustic source term from the Tam-Auriault (TA) jet-noise model were analyzed. Results indicated that the WIW treatment advances the onset of jet flow instability in the shear-layer, leading to the early breakdown of jet shear-layer and production of different scales of downstream turbulent structures. As a result, the distribution and production of turbulent kinetic energy are affected, and the generation and emission of jet noise are controlled. The WIW treatment enables the control of fine scale turbulence, resulting in the reduction of mid- to high-frequency noise in the far field, while ensuring a low thrust loss. This feature makes the WIW method a promising approach for jet noise control.

Keywords: Jet noise, Wavy inner wall, Noise control, Large eddy simulation

1 Introduction

In recent years, increasingly stringent environmental regulations have placed significant pressure on the suppression of aviation noise. Though researchers have made great strides in reducing jet noise from airliners, significant noise is still observed during takeoff [1], making jet noise control a more challenging task than ever. The main component of jet noise is the turbulent mixing noise at the end of the potential core, which carries two main components: large-scale turbulent structures and fine-scale turbulence. The length scales of the potential core and turbulent structures are crucial for noise emission, and various jet noise control methods have been proposed to address them [2–5]. These methods can be categorized into passive and active control methods. Passive methods involve changing the shape of the nozzle trailing edge

and nozzle type, such as corrugated nozzles [2] and chevron nozzles [3], which alter the jet shear layer and turbulent structures. In contrast, active methods use microjets to improve jet mixing, such as fluid injection nozzle technology [4] and water jet technology [5], which control the nozzle area and thrust vector to achieve noise and thrust control. However, the need for additional devices has hindered the widespread application of these methods, and most active control methods remain in the experimental stage.

Passive control methods aimed at reducing jet noise at the exit of the nozzle have proven to be simple and effective. Aharon and Ahuja [6] found that the fully developed boundary layer can contribute to higher levels of jet noise, and altering the shape of the nozzle trailing edge can modulate the magnitude of the noise radiation. Bradbury and Khadem [7] demonstrated that installing a small rectangular tab at the nozzle can accelerate velocity attenuation, shorten the length of the potential core, and significantly reduce jet noise. Bridges and Brown [3] proposed the use of chevron nozzles as an effective method for suppressing jet noise. By altering parameters such as the number, penetration degree, and length of the chevrons, they were able to weaken and suppress large-scale vortex structures and strengthen the mixing of shear layers, leading to noise reduction. The chevron nozzle is particularly advantageous in high bypass ratio engines as it incurs a relatively low thrust loss. However, it is still necessary to develop a noise reduction method that can guarantee engine thrust without additional equipment.

The wavy wall is a widely used flow control technique to reduce flow drag, and several studies have been conducted on its drag reduction capabilities [8–13]. However, there has been limited research on the performance and mechanisms of wavy wall in suppressing jet noise. Meng et al. [12] conducted large eddy simulations of low-speed turbulent flow and found that the spanwise wavy wall can generate additional noise. Passing through the wavy wall generates a more stable free shear shedding by the wall surface than the smooth one, which results in a suppressing effect on low-frequency sound sources. Chen et al. [14] investigated the mechanisms of drag and noise reduction of the wavy cylinder and found that the pressure fluctuation on the wavy cylinder surface is suppressed, resulting in a significant reduction of the lift coefficient fluctuation. The overall sound pressure level (OASPL) of far-field noise radiated by the wavy cylinder is reduced, and the tones are significantly suppressed or eliminated. Chen et al. [15] applied the wavy wall to treat the cove inner-wall of the 30P30N airfoil, and their results showed that low-frequency narrowband tonal noise was significantly suppressed while maintaining the aerodynamic performance. The wavy wall control method induces very small geometrical modifications, which introduces a trivial sacrifice in thrust while enhancing shear layer mixing. As a result, the wavy wall is a promising method for flow and noise control for subsonic jets.

In this study, we investigate the effectiveness of the wavy inner-wall (WIW) treatment as a passive control method for reducing jet noise. A parametric study is conducted to examine the characteristics of this approach. The article is organized as follows: In Section 2, we introduce the numerical methods used in this study. Section 3 describes the computational conditions and the method validations. Section 4 compares the results and analyzes the effect of the WIW treatment on the jet flow field and reveals the mechanism of noise suppression. Conclusions are summarized in Section 5.

2 Governing equations

The hybrid CFD/CAA method is used to study flow and sound fields of the baseline and the WIW-treated nozzles. The LES method, which has been proved to be a robust tool for the prediction of the jet noise [16–19], is applied in the near field. And the Ffowcs Williams and Hawkings [20] (FW-H) integration is used for far field prediction. This method is relatively mature for the prediction of jet noise [21–25], although the contamination of the turbulent wake is still unresolved.

2.1 Favre-filtered Navier–Stokes equations for flow simulations

The Favre filtering [26] is applied to the three-dimensional Navier–Stokes equations. This results in flow prediction under the LES framework. The continuity, momentum and energy governing equations are written as

$$\frac{\partial \overline{\rho}}{\partial t} + \frac{\partial \left(\overline{\rho}\widetilde{u}_i\right)}{\partial x_i} = 0, \tag{1}$$

$$\frac{\partial}{\partial t}\left(\overline{\rho}\widetilde{u}_i\right) + \frac{\partial}{\partial x_j}\left(\overline{\rho}\widetilde{u}_i\widetilde{u}_j\right) + \frac{\partial \overline{p}}{\partial x_i} - \frac{\partial \widetilde{\sigma}_{ij}}{\partial x_j} = -\frac{\partial \tau_{ij}}{\partial x_j} + \frac{\partial}{\partial x_j}\left(\overline{\sigma}_{ij} - \widetilde{\sigma}_{ij}\right), \tag{2}$$

$$\frac{\partial\left(\overline{\rho}\widetilde{e} + \overline{\rho}\widetilde{u}_i\widetilde{u}_j/2\right)}{\partial t} - \frac{\partial}{\partial x_j}\left(\widetilde{\sigma}_{ij}\widetilde{u}_i\right) + \frac{\partial \widetilde{q}_i}{\partial x_i} + \frac{\partial\left[\left(\overline{\rho}\widetilde{e} + \overline{\rho}\widetilde{u}_i\widetilde{u}_j/2 + \overline{p}\right)\widetilde{u}_i\right]}{\partial x_i} = RHS_{\mathrm{E}}, \tag{3}$$

where the overbar, $\bar{}$, stands for spatial average, the tilde, $\tilde{}$, for Favre filtering, t for time, and x_i for the Cartesian coordinates. The variables ρ, u_i, p and e denote the density, velocity component, pressure and internal energy, respectively. In Eq. (2), τ_{ij} is the subgrid-scale stress, $\overline{\sigma}$ the filtered viscous stress tensor, and $\widetilde{\sigma}$ the viscous stress tensor with parameters of filtration rate and temperature. In Eq. (3), $\widetilde{q}_i$ is the heat flux. The equations of τ_{ij}, $\widetilde{\sigma}$ and $\widetilde{q}_i$ are shown in Eqs. (4, 5, and 6), respectively. In Eq. (6), Pr is the Prandtl number. RHS_{E} consists of seven terms as given in Ref. [27].

$$\tau_{ij} = \overline{\rho}\left(\widetilde{u_i u_j} - \widetilde{u}_i\widetilde{u}_j\right), \tag{4}$$

$$\widetilde{\sigma} = \mu\left(\overline{T}\right)\left(\frac{\partial \widetilde{u}_i}{\partial x_j} + \frac{\partial \widetilde{u}_j}{\partial x_i} - \frac{2}{3}\frac{\partial \widetilde{u}_k}{\partial x_k}\delta_{ij}\right), \tag{5}$$

$$\widetilde{q}_i = -\frac{\mu\left(\widetilde{T}\right)C_p}{Pr}\frac{\partial \widetilde{T}}{\partial x_i}. \tag{6}$$

These equations are closed by the equation of state, $\widetilde{p} = R\overline{\rho}\widetilde{T}$, where $R = 287.1\,\mathrm{J/(kg \cdot K)}$. The dynamic Smagorinsky-Lilly model is used to calculate the subgrid-scale stress using the equation

$$\tau_{ij} - \frac{1}{3}\tau_{kk}\delta_{ij} = -2\mu_t\overline{S}_{ij}, \tag{7}$$

where, μ_t is the subgrid-turbulent viscous force, τ_{kk} is a part of the subgrid-scale isotropy, $\overline{S}_{ij}$ is the deformation rate tensor calculated from the velocity field $\widetilde{u}_i$. μ_t and $\overline{S}_{ij}$ are shown in Eqs. (8, 9).

$$\mu_t = \rho L_s^2 |\overline{S}|, \tag{8}$$

$$\overline{S}_{ij} = 0.5\left(\frac{\partial \widetilde{u}_i}{\partial x_j} + \frac{\partial \widetilde{u}_j}{\partial x_i}\right), \tag{9}$$

where, $|\overline{S}| = \sqrt{2\overline{S}_{ij}\overline{S}_{ij}}$, and L_s is the mixing length of the grid, $L_s = min\left(\kappa d, C_s V^{1/3}\right)$, where κ is the von Kármán constant, d is the distance to the nearest wall, $V^{1/3}$ is the local grid scale, and C_s in the dynamic Smagorinsky-Lilly model is dynamically calculated based on the information provided by the resolved flow scales.

2.2 Ffowcs Williams and Hawkings equation for far field noise

For the calculation of far-field noise, Farassat's formulation [28] for Ffowcs Williams and Hawkings (FW-H) equations [20] is used. This is a retard time method for acoustic analogy prediction, which can be written in terms of acoustic pressure $p^{'}$ in the following form:

$$\left(\frac{1}{c^2}\frac{\partial^2}{\partial t^2} - \frac{\partial^2}{\partial x_i^2}\right)p^{'}(x,t) = \frac{\partial}{\partial t}\left[\rho_0 v_n \delta(f)\right] - \frac{\partial}{\partial x_i}\left[p n_i \delta(f)\right] + \frac{\partial^2}{\partial x_i \partial x_j}\left[H(f) T_{ij}\right], \tag{10}$$

where c and ρ_0 are the speed of sound and the freestream fluid density; v_n is the local normal velocity of the surface, and p is the local gage pressure on the surface; $\delta(f)$ and $H(f)$ are the Dirac delta and the Heaviside functions. The Lighthill stress tensor is defined as

$$T_{ij} = \rho u_i u_j - \sigma_{ij} + \left(p^{'} - c^2 p^{'}\right)\delta_{ij}, \tag{11}$$

where δ_{ij} is the Kronecker delta and σ_{ij} is the viscous stress tensor. Formula 1A of Farassat was used to solve the FW-H equation, and the complete solution consists of surface integrals and volume integrals. The surface integrals represent the contributions from monopole and dipole sources and part of the effect of quadrupoles on the surface. The contribution of the volume integrals becomes small when the source surface encloses the source region. Thus, the volume integrals were dropped when applying penetrable integral surfaces. This resulted in the thickness and loading terms of Farassat's Formula 1A being expressed as

$$p_T^{'}(\boldsymbol{x},t) = \frac{1}{4\pi}\int_{f=0}\left[\frac{\dot{v}_n}{r(1-M_r)^2}\right]_{ret}\rho_0 dS + \frac{1}{4\pi}\int_{f=0}\left[\frac{v_n\left(r\dot{M}_r + c_0\left(M_r - M^2\right)\right)}{r^2(1-M_r)^3}\right]_{ret}\rho_0 dS, \tag{12}$$

$$\begin{aligned} p_L^{'}(\boldsymbol{x},t) = {} & \frac{1}{4\pi}\int_{f=0}\left[\frac{\dot{L}_r}{c_0 r(1-M_r)^2}\right]_{ret} dS + \frac{1}{4\pi}\int_{f=0}\left[\frac{L_r - L_M}{r^2(1-M_r)^2}\right]_{ret} dS \\ & + \frac{1}{4\pi}\int_{f=0}\left[\frac{L_{rn}\left(r\dot{M}_r + C_0\left(M_r - M^2\right)\right)}{c_0 r^2(1-M_r)^3}\right]_{ret}\rho_0 dS. \end{aligned} \tag{13}$$

An advanced time approach [29] is adopted to obtain an increased efficiency of the numerical algorithms.

3 Computational setup and validation

3.1 Nozzle model

As shown in Fig. 1, the axisymmetric nozzle NASA SMC000 [30] was used as the baseline. This nozzle has an exit diameter of 2 inches ($D_j = 0.0508$ m) and a 6-inch inlet. The inlet is followed by a 27° contraction section, and this contraction ratio is reduced to a 5° taper near the nozzle exit. The present study focuses on the cold jet condition. The operating condition in this paper is the set-point 7 (SP7) in the experiment [31], and the flow conditions are shown in Table 1 (The centerline velocity is applied to calculate the Reynolds number). Based on a recent study of the same benchmark [32], a posteriori estimate of the relevant boundary layer thickness for the SP7 condition gives $\delta = 0.0128D_j$.

A passive noise control method, termed the wavy inner wall (WIW) treatment, is applied to the baseline model. It is expected to control the flow structures around the nozzle and enhance the shear layer mixing to achieve noise suppression without great geometrical modifications on the nozzle. Parametric studies were conducted to locate the key factors for the WIW treatment. The wavy wall is defined by the amplitude $h = aD_j$ and the wavelength $\lambda = bD_j$, where D_j denotes the diameter of the nozzle exit. a and b are constants to be designed. The inner wall shape of the nozzle shown in Fig. 2 is given by the following formula:

$$\begin{aligned} W(x,y) = \left[W_0(x,y) + h\right] + h\sin\left\{\tfrac{2\pi}{\lambda}\left[X(s) - X_0(s)\right]\right\} \cdot n(x,y), \\ X_0(s) \le X(s) \le X_1(s), \end{aligned} \tag{14}$$

where $W_0(x,y)$ denotes the profile of the inner wall, $X(s)$ denotes the coordinate along the wavy shape of the inner wall, $X_0(s)$ and $X_1(s)$ are the start- and the end-point on the curve, respectively. $n(x,y)$ is the outward normal unit vector.

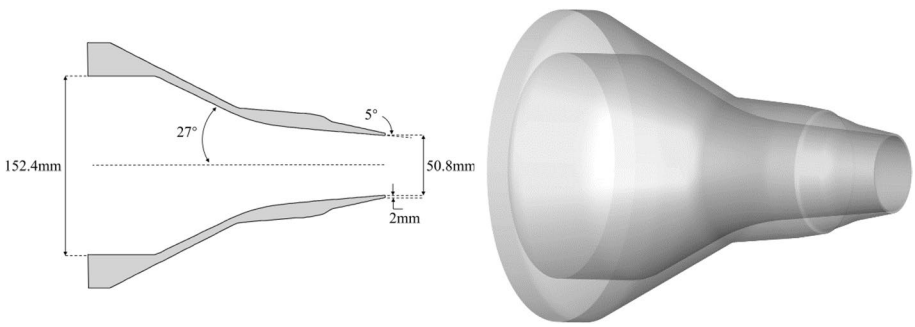

Fig. 1 Geometry of the NASA SMC000 nozzle

Table 1 Operating conditions of the NASA SMC000 nozzle at set-point 7

Set Point	*Ma*	Jet Reynolds number based on D_j	T_j/T_∞	NPR[a]
7	0.9	1×10^6	0.835	1.861

[a] *NPR* Number of Pressure Ratio

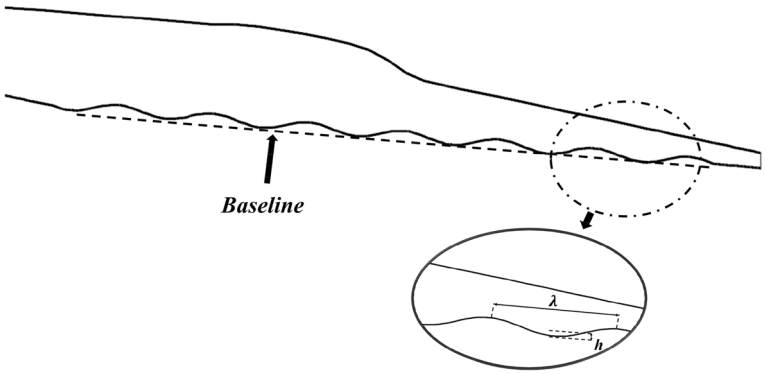

Fig. 2 Sketch of the WIW treatment

3.2 Numerical setup

The compressible Favre-averaged Navier–Stokes equations were solved by the finite volume method. The convective and viscous fluxes were discretized by the cell-centered third order monotone upstream-centered scheme for conservation laws (MUSCL) [33]. An implicit second order dual time-stepping method is utilized for the time discretization [34]. In order to avoid excessive numerical simulation, a multigrid method is adopted to speed up the iteration [35].

As shown in Fig. 3, the origin is located at the center of the nozzle exit. The computational domain was set to be $x/D_j \in [-10, 75]$ along the x-axis, and to be $r/D_j \in [0, 45]$ along the r-axis. Structured asymmetric mesh was applied. An O–H mesh topology was used to resolve the nozzle structure. A refined zone which extends downstream of the nozzle exit from $(x/D_j = 0; r/D_j = 2)$ to $(x/D_j = 25; r/D_j = 5)$ was set for improving flow resolution. In this zone, the mesh size has a maximum of $\Delta x_{max} = \Delta r_{max} = 1.8\,\text{mm}$ which enables to resolve acoustic waves up to the Strouhal number $St \approx 2$ with 12 points per wavelength. The axisymmetric ambient mesh was generated by rotating from a two-dimensional grid, and the number of rotating steps n_θ is 120. This results in the grid as shown in Table 2 and Fig. 4.

Given the total temperature and total pressure, the pressure inlet boundary condition was applied. Adiabatic no-slip wall boundary conditions were adopted for both the inner

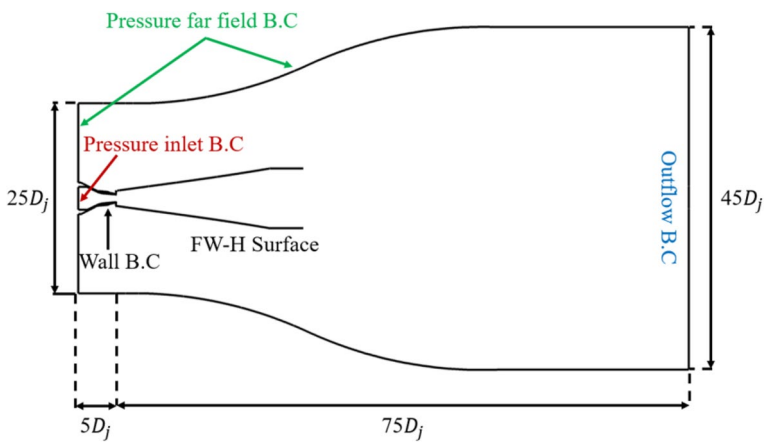

Fig. 3 Schematic view of the computational domain and boundary conditions

Table 2 Parameters of the grid

Grid points	n_θ	$\Delta x/D_j$ at $x = 0$	Growth rate $\partial\Delta x/\partial x$	$\Delta r/D_j$ at $r = D_j/2, x = 0$	Growth rate $\partial\Delta r/\partial r$
10M	120	0.01	1.01	0.002	1.01

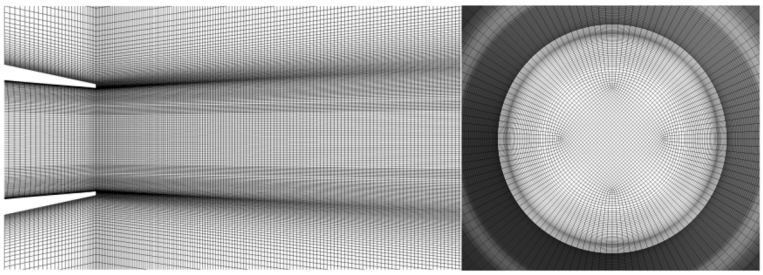

Fig. 4 Mesh profiles for the baseline SMC000 nozzle

and the outer nozzle walls. Out-flow boundary condition with non-reflective treatment based on one-dimensional flows was applied at the jet exit. Non-reflecting boundaries were also applied for the upstream and the surrounding far field. The inflow turbulence is given by an empirical formula, which is

$$I = \frac{u^{'}}{u_{avg}} \approx 0.16 Re_H^{-\frac{1}{8}}, \tag{15}$$

$$l_{turb} \approx \frac{0.07H}{C_\mu^{3/4}}, \tag{16}$$

where C_μ is 0.09, and H denotes the nozzle diameter.

Based on the mesh configuration, the time step was set to five thousandth of the reference time $t^* = D_j/U_j$, which satisfies CFL < 1, and U_j is the time-averaged jet speed at the center of the nozzle exit. As suggested in Ref. [37], the simulations were run for $200t^*$ to remove the initial solution transients. Then, the flow field is counted for more than $300t^*$ to extract information for turbulence calculation and the far-field FW-H integration.

3.3 Validation for the baseline case

In order to verify the accuracy of the numerical simulation, the results of the baseline SMC000 nozzle were compared with the experimental data available in the NASA SHJAR database (operating condition SetPoint7). The time-averaged unsteady results of the axis and the lip-line (such as mean velocity and fluctuating velocity), and the far-field noise results (such as overall sound pressure level directivity and one-third octave) are compared with the results of literature [30, 36, 37].

The cold jet flow corresponding to SetPoint7 in the NASA SHJAR database has a very long jet core region length and a very thin initial shear layer. It has been very challenging to accurately capture the flow structures. This challenge is greatly increased for further noise prediction. Nevertheless, we managed to capture the essential flow structures under mild computational costs.

Figure 5 shows the jet centerline profiles of mean axial flow velocity and axial velocity fluctuations. In Fig. 5a, consistency is observed with the results in the literature, though there still exist some discrepancies with the experiments. The length of the jet plume is slightly underestimated, but the downstream velocity decay trend is consistent with the experiment. In Fig. 5b, though the peak remains earlier than the experiments due to shorter estimated jet plume, the self-similarity region after the peak fluctuations is also properly resolved. Figure 6 shows the axial velocity and velocity fluctuations along the lip-line. As shown in Fig. 6a, the mean velocity at the lip-line is slightly lower than the experimental value, but the overall attenuation trend is consistent. The velocity fluctuations shown in Fig. 6b agree well with the LES results from Angelino [37] and show reasonable agreement with the experiments.

Power spectra of velocity magnitude were calculated at two positions P1–P2. Indicated by the Fourier spectra in Fig. 7, fluctuations in the turbulent kinetic energy are captured over four orders of magnitude using this numerical configuration. As shown in Fig. 7a, the power spectrum at P1 shows a strong discrepancy with the isotropic turbulence that holds a -5/3 pattern in the power spectrum. This is because the turbulence mixing is not fully developed at P1, resulting in strong non-isotropic turbulence. The spectrum

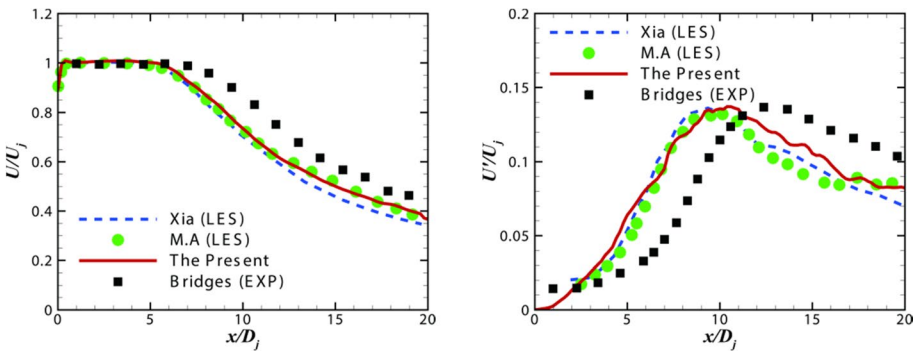

(a) mean axial flow velocity (b) fluctuations of axial velocity

Fig. 5 Jet centerline axial flow velocity profiles: **a** mean flow velocity; **b** velocity fluctuations. Comparisons are made with LES results from Xia [36] and Angelino [37]

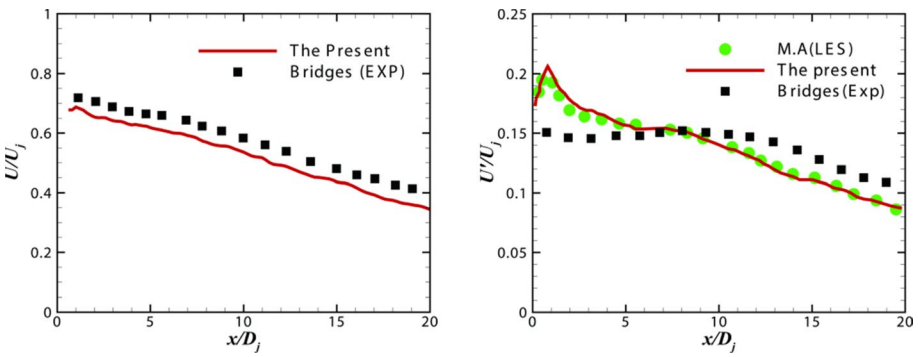

(a) mean axial flow velocity (b) fluctuations of axial velocity

Fig. 6 Jet lip-line axial flow velocity profiles: **a** mean flow velocity; **b** velocity fluctuations. Comparisons are made with LES results from Angelino [37]

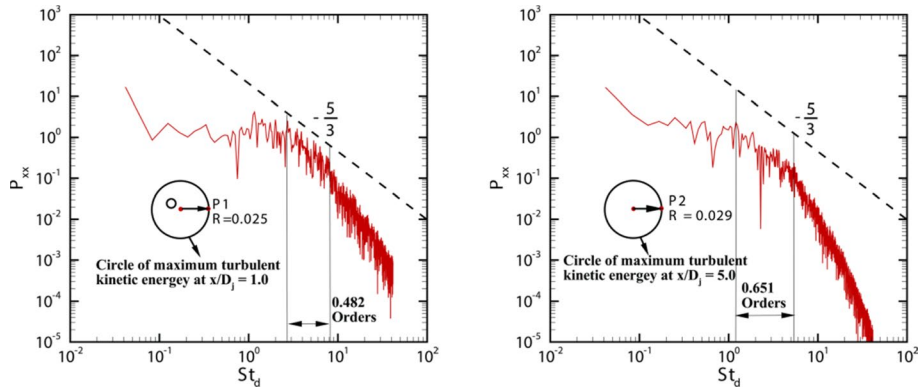

(a) Spectrum at P1 (b) Spectrum at P2

Fig. 7 Power spectra of velocity magnitude at two positions in the jet shear-layer: **a** P1 with $x/D_j = 1.0$, $r/D_j = 0.5$; **b** P1 with $x/D_j = 5.0, r/D_j = 0.5$

amplitude reduces as the flow travels downstream, meanwhile, the frequency range that satisfies the -5/3 characteristics is enlarged from 0.482 orders to 0.651 orders (the non-dimensional frequency, $St = fD_j/U_j$). This implies that the jet turbulence has developed to a new level at this stage.

Figure 8 shows the far-field noise directivity measured by the overall sound pressure level (OASPL). Observers are distributed along the circle centered at the nozzle center with a radius of $100D_j$. The observer angle along the jet axis is set to be 0° for the downstream. Good agreement with the experiment is achieved except for locations with angles smaller than 40°. This error is explained by the outflow treatment to avoid jet wake interference during the FW-H integration. The averaged OASPL error for observers with angles greater than 40° is about 3 dB. Figure 9 shows the 1/3 octave spectrum of the observer at 90°. When compared with the experiment,

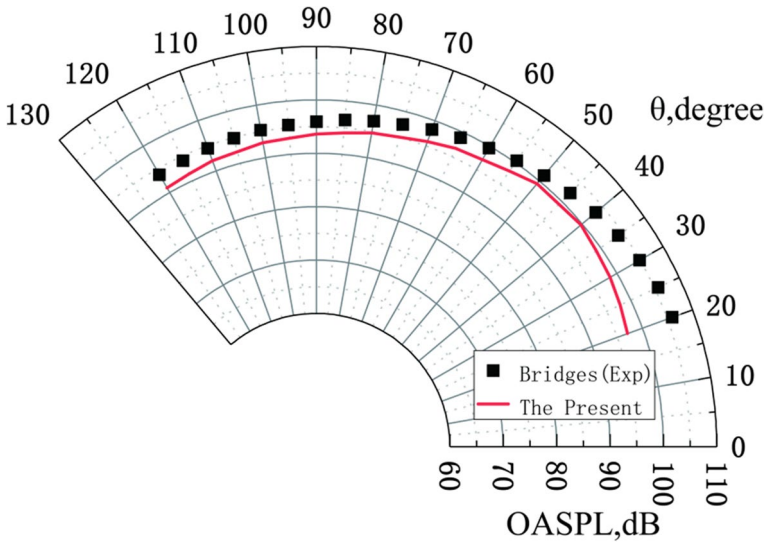

Fig. 8 The far-field directivity

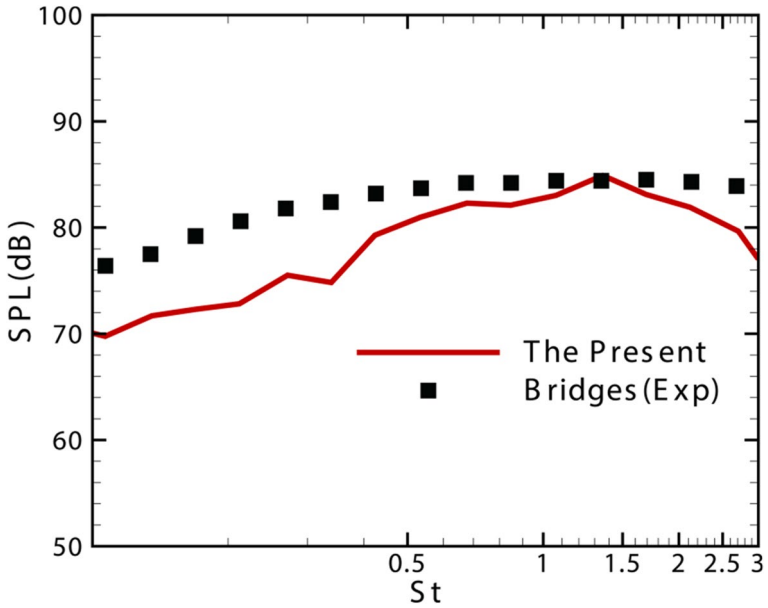

Fig. 9 1/3 octave spectrum at 90°

reasonable agreement is achieved with small discrepancies observed near the dominant frequencies.

The above comparisons show that the numerical method we used is able to reasonably capture the turbulent flows (sound source) and the far-field sound radiation of jet flows. Consequently, this numerical configuration is applied for evaluation of the WIW-treated nozzles and for further parametric studies under the same operating condition (SP7).

Two different wave patterns are designed to find a proper initial shape of the wavy inner wall. The nozzle in Case 1 carries a large wave pattern, while that in Case 2 is treated with a small wave pattern. The wave height of Case 1 is the boundary layer thickness $\delta = 0.0128D_j$, and the wave height of Case 2 is $\frac{1}{2}\delta = 0.0064D_j$. The distribution range of waves in Case 1 is $2D_j$ from the nozzle exit, and that in Case 2 is $1D_j$. Figure 10 shows the corresponding models. The detailed parameters of the WIW treatment are given in Table 3.

4 Results of the initial WIW-treated nozzles

4.1 Turbulent flows

The distributions of the mean axial velocity and the velocity fluctuations at the centerline downstream of the nozzle exit are shown in Fig. 11. Comparing the two WIW-treated nozzles with the baseline, as shown in Fig. 11a, Case 1 has a shorter potential core and the axial velocity decreases faster. While, Case 2 is almost the same with the baseline. The scales of the potential core are listed in Table 4. Figure 11b shows the distribution of velocity fluctuations. The WIW-treated cases reach the peak earlier than the baseline nozzle. This implies that the turbulence mixing is enhanced by the WIW treatment, and it will be, as discussed later, reflected in the difference in the far-field sound radiation. This effect is much stronger in Case 1 than in Case 2.

The distributions of the mean axial velocity and the velocity fluctuations along the radial direction at different streamwise locations are shown in Fig. 12. The differences of the mean

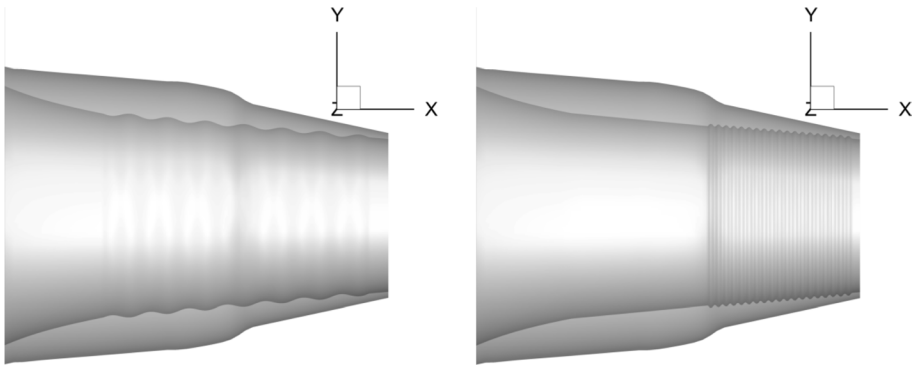

(a) Case 1 (b) Case 2

Fig. 10 Design of the WIW-treated nozzles: **a** Case 1 with a large and long-paved wave pattern; **b** Case 2 with a small and short-paved wave pattern

Table 3 Geometric parameters of two WIW-treated nozzles

Wave type	h/D_j	λ/D_j	h/λ
Case 1	0.0128	0.25	0.0512
Case 2	0.0064	0.05	0.128

axial velocity between the three nozzles are small at the nozzle exit. This implies that the jet thrust is maintained under the WIW treatment. As for the velocity fluctuations, opposite effects are observed in Case 1 and Case 2 when compared with the baseline. This implies that different wave patterns may have opposite effects on the initial shear layer.

The development of the shear layer instability directly affects the turbulent characteristics of jet flows, which is of great significance to investigate the subsonic jet noise mechanism. Figure 13 shows the variation trend of the jet half-width value along the axial direction, where the jet half-width value is expressed as

$$U(x, r_{0.5}(x)) = 0.5U(x, 0). \tag{17}$$

The half-width value shows the expansion trend of the jet. In the potential core, the effect of the WIW-treated nozzles is small, while, at the end of the potential core, the WIW treatment leads to a rapid expansion of jet flow. The expansion rates of the two

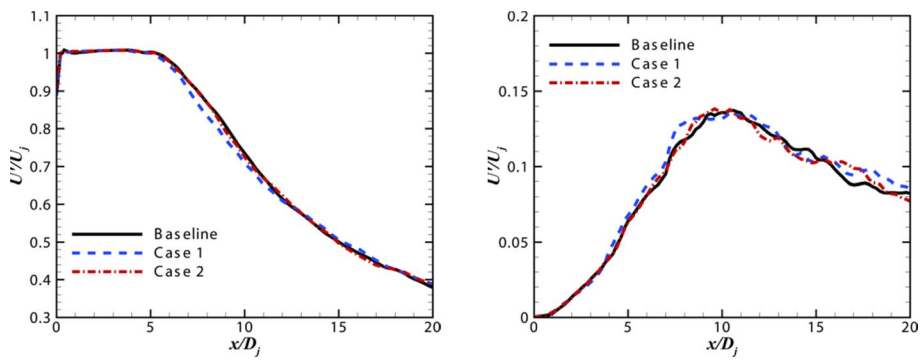

(a) mean axial flow velocity (b) fluctuations of axial velocity

Fig. 11 Jet centerline axial flow velocity profiles: **a** mean flow velocity; **b** velocity fluctuations

Table 4 The potential core length

Model	Baseline	Case 1	Case 2
Potential core length	$6.6D_j$	$6.2D_j$	$6.5D_j$

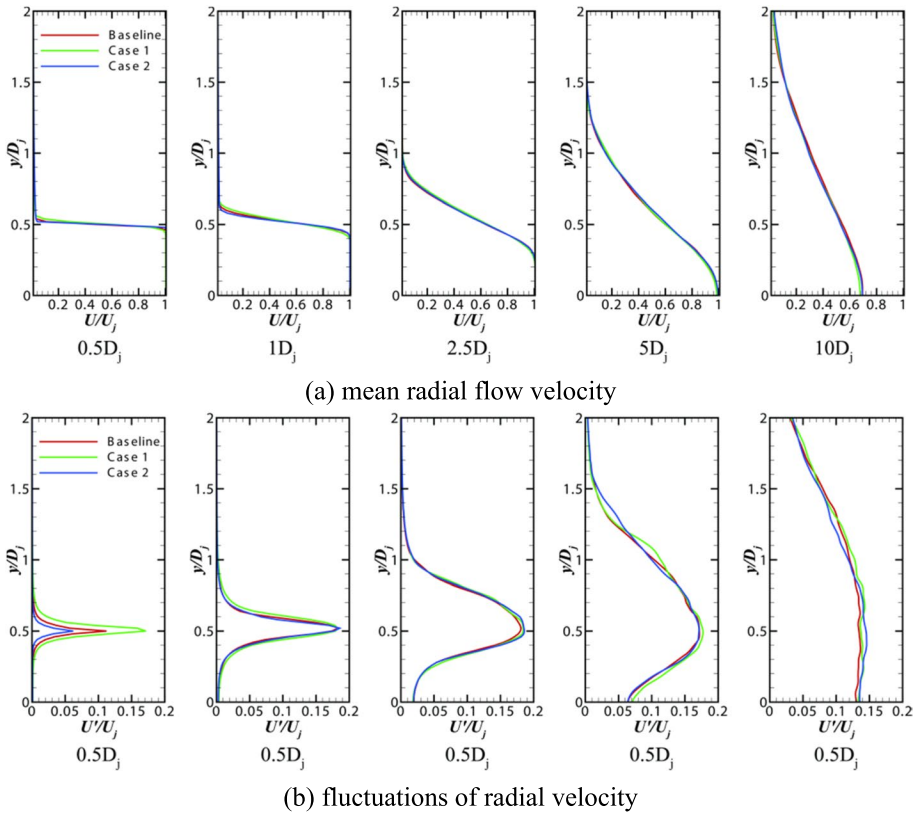

Fig. 12 Jet radial velocity profiles at locations $x/D_j = 0.5$, 1, 2.5, 5 and 10: **a** mean flow velocity; **b** velocity fluctuations

WIW-treated nozzles are almost same ($dr_{0.5}/dx \approx 0.077$), which are larger than the expansion rate of the baseline ($dr_{0.5}/dx \approx 0.073$). The WIW enhances the mixing effect of the jet shear layer, accelerates the expansion rate of the jet, and affects the large-scale coherent structure in the mixing region of the jet turbulence.

Figure 14 shows the variation trend of the shear layer thickness along streamwise, where the shear layer thickness δ is,

$$\delta = r_{0.1} - r_{0.95}, \tag{18}$$

where, $r_{0.1}$ and $r_{0.95}$ represent the radial position corresponding to 0.1 and 0.95 of the axial velocity at the centerline. It is obvious that the shear layer thickness increases with the development of the jet flow downstream. For the baseline and Case 2, the growth trend of the shear layer thickness is similar, and the slope shows a single linear change. For Case 1, there are two difference growth trends in the shear layer thickness. The first

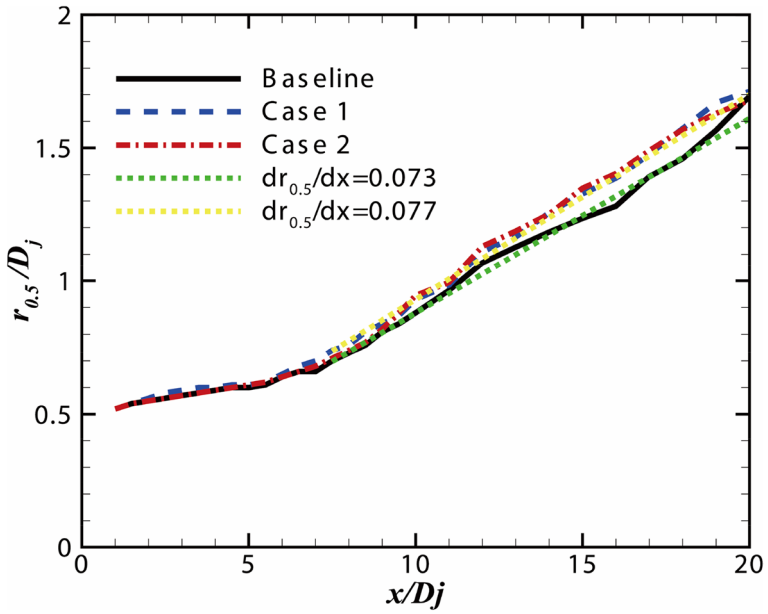

Fig. 13 Jet half-width value

stage as the potential core, its growth trend is consistent with the baseline and Case 2, and the shear layer thickness value is larger. However, the growth rate decreases in the downstream of the potential core, and the shear layer thickness is smaller than others. This implies that Case 1 increases the thickness of the shear layer within the potential core, while decreases the thickness of the shear layer behind the potential core. The effects on noise are reflected in the difference in the far-field sound radiation.

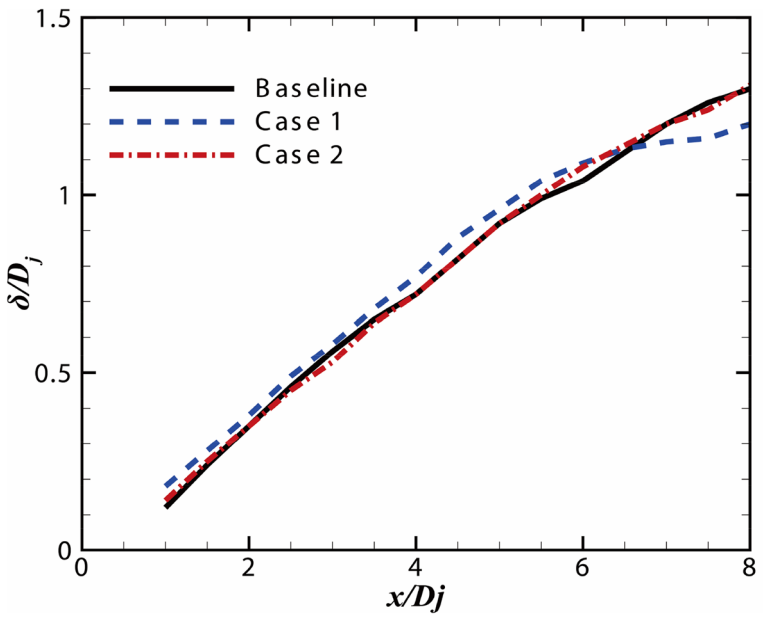

Fig. 14 Jet shear layer thickness

Figure 15 compares the vortex structure of the instantaneous flow field of different nozzles. The Q-criterion iso-surfaces are used to describe vortical jet flows. By comparing the baseline with two WIW-treated nozzles, the main difference resides in the generation, evolution and breaking-down of the ring-shaped vortex structures near the nozzle exit. Before the breaking-down of such vortices, the Kelvin–Helmholtz (K-H) instability of jet-mixing is developed through a distance of about $0.96D_j$ in the baseline case. While, as shown in Fig. 15b-c, the K-H instability is accelerated by the WIW treatment, resulting in a significant reduction in the breaking-down distance. As listed in Table 5, greater influence is observed in Case 1 than in Case 2. This indicates that the large and long-paved wave pattern will, as expected, trigger stronger flow instability. The breaking-down position of the ring-shaped vortices can be advanced for up to 50% in the WIW-treated nozzle.

Figure 16 shows the vorticity magnitude at the three axial-cut planes. The enhancement of flow mixing by the WIW treatment is revealed by the development of the ring-shaped structures along the jet axis. The effect on the trigger of instability by the WIW treatment is observed between $0.5D_j$ and $1D_j$. Then, the ring-shaped structures are transformed to fully turbulent ones after $5D_j$. At this stage, the vortical flows are significantly confined to a smaller region in the WIW-treated nozzles. This feature implies the WIW treatment has the potential of noise control, because the size of the jet flow region is a key factor related to jet noise.

By the analysis of the time averaged flow field and the instantaneous flow field, it shows that the WIW-treated nozzles have less influence on the flow field velocity; especially the flow field velocity distribution of the Case 2 is similar with the baseline. This may indicate that the WIW treatment has less effect on the thrust of the engine.

4.2 Sound field

4.2.1 The near-field

Figure 17 shows the distribution of density gradient and vorticity of the baseline and the WIW-treated nozzles. The contour of density gradient reveals the generation and

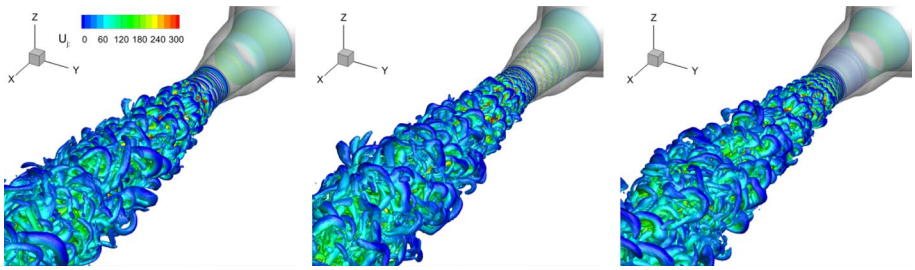

(a) Baseline (b) Case 1 (c) Case 2

Fig. 15 Iso-surface of $Q = 5\left(U_j^2/D_j\right)$ at $t = 500t^*$, colored by axial jet velocity: **a** Baseline; **b** Case 1; **c** Case 2

Table 5 Breaking-down locations of jet shear layer

Model	Baseline	Case 1	Case 2
Axial locations[a]	$0.96D_j$	$0.48D_j$	$0.75D_j$

[a] The breaking-down position is defined as the location of vortex merging based on $Q = 5\left(U_j^2/D_j\right)$

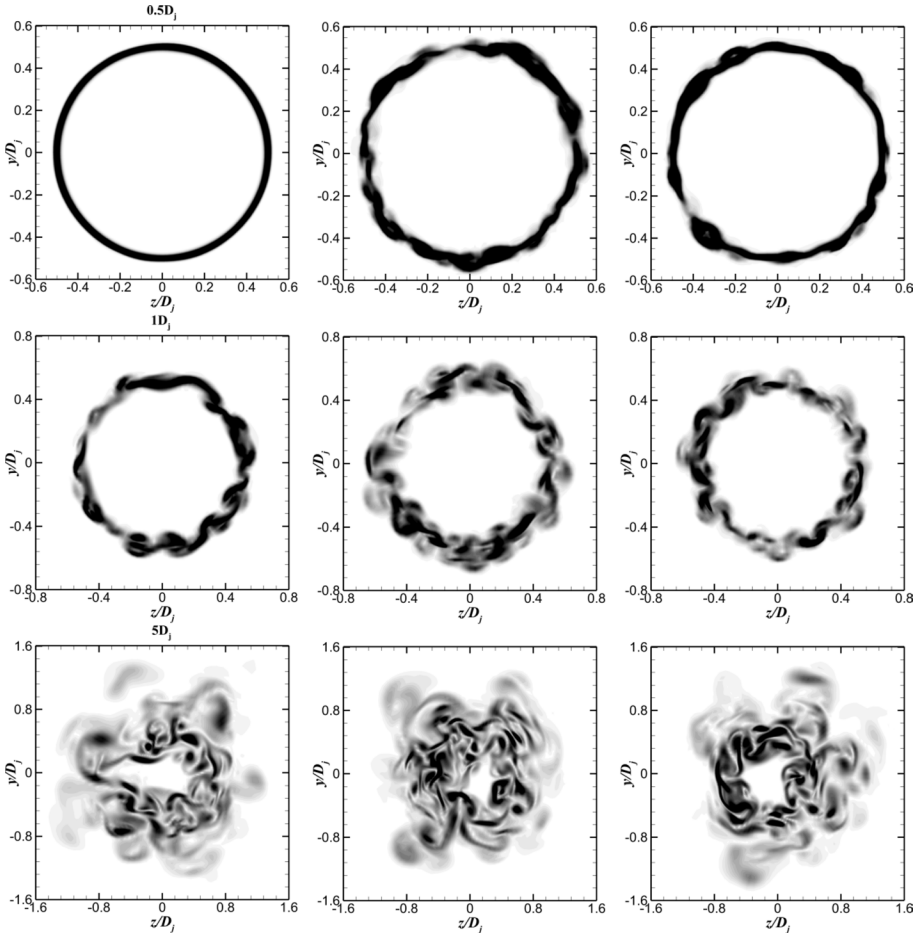

(a) Baseline (b) Case 1 (c) Case 2

Fig. 16 Vorticity magnitude contours on the YOZ plane at $x/D_j = 0.5,\ 1,$ and 5 (from top to bottom): **a** Baseline; **b** Case 1; **c** Case 2. The color scales range up to the level of $16U_j/D_j$ for vorticity

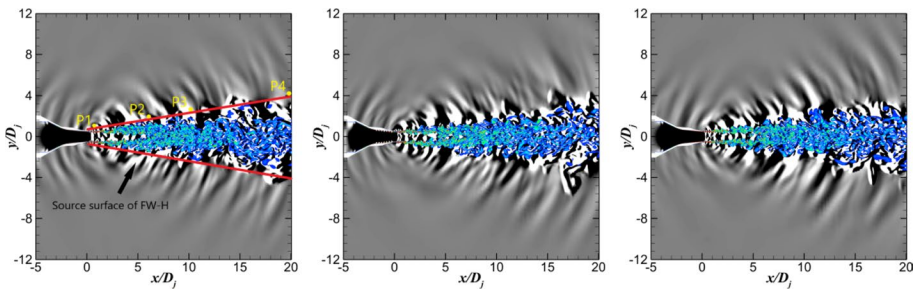

(a) Baseline (b) Case 1 (c) Case 2

Fig. 17 Flow and sound near-field visualized by density gradient (greyscale) and vorticity. The color scales range up to the level of $8U_j/D_j$ for vorticity, and from -10 to 10 for density gradient: **a** Baseline; **b** Case 1; **c** Case 2

propagation of jet noise. Two main radiation directions are observed for the three nozzles. The downstream propagating noise component takes most of the acoustic energy. Another peak of sound radiation is the upstream along the jet surface. This directivity

is consistent with the experiment and is a typical feature of subsonic jets. The radiation angle of the maximum acoustic disturbance is around 30° (downstream). A slight difference is observed among the three cases.

In order to achieve detailed observation of the near-field acoustic characteristics, four monitoring points, P1–P4, were set along the FW-H integral surface as shown in Fig. 17a. Coordinates of such points, normalized by the jet diameter, are P1 ($x/D_j = 0.5$, $y/D_j = 1.08$, $z/D_j = 0$), P2 (6, 1.82, 0), P3 (10, 2.37, 0), and P4 (20, 3.91, 0). These four points represent the jet exit, the end of the potential core, the large-scale turbulent region and the end of jet, respectively. As shown in Fig. 18a, stronger pressure fluctuations are observed near the nozzle exit, P1 (0.0254, 0.055, 0), due to the disturbances introduced by the WIW treatment. This pattern is gradually reversed as the flow travels downstream. The spectra are lowered-down by up to 6 dB in Case 1 and Case 2 at P4. Meanwhile, the spectra with a narrow-band peak observed near $St = 0.6$ at P1 are transformed to pure broadband spectra with acoustic energy focused at the low frequency. The WIW treatment mainly functions in the low frequency range.

Detailed OASPL difference referred to the baseline is shown in Fig. 19. Case 2 introduces less OASPL increase at the nozzle exit and more OASPL decrease after the "turning point" between $0.5D_j$ to $6D_j$. Thus, Case 2 is a better configuration for the control of jet noise.

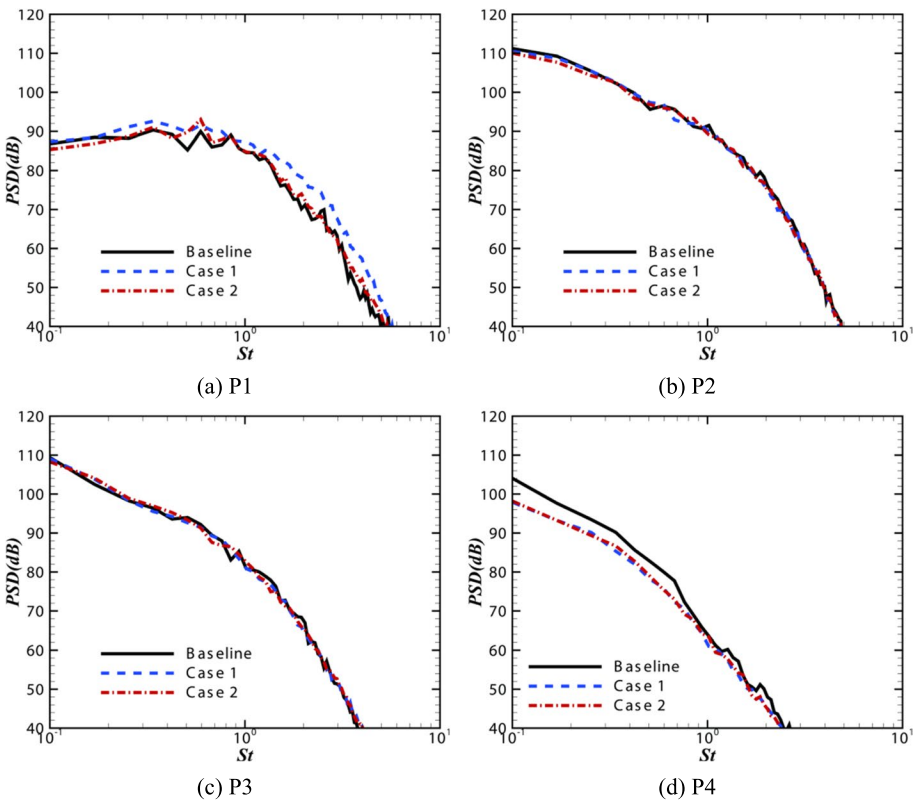

Fig. 18 Power spectrum density of sound pressure at four observers: **a** P1 ($x/D_j = 0.5$, $y/D_j = 1.08$, $z/D_j = 0$); **b** P2 (6, 1.82, 0); **c** P3 (10, 2.37, 0); **d** P4 (20, 3.91, 0)

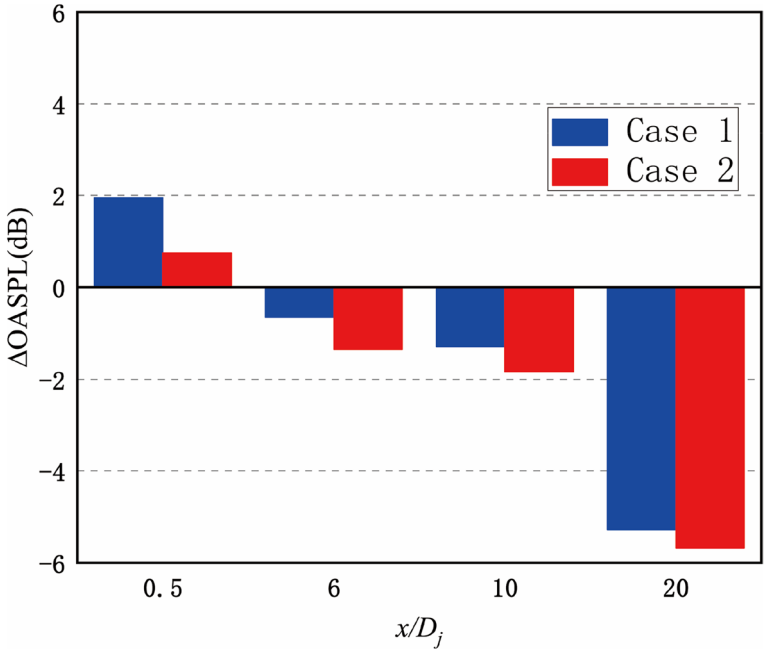

Fig. 19 The difference of OASPL at monitoring points P1–P4

4.2.2 The far-field

Since the permeable FW-H approach is used for the far-field noise, it is necessary to make the integral surface cover the sound sources as much as possible. In the meanwhile, the turbulent wake should be excluded from the permeable source surface. Thus, an FW-H surface is created as illustrated in Fig. 20 (see also Fig. 17a). The FW-H integral surface is $25D_j$ in axial length, and has diameters of around $2D_j$ and $8D_j$ at its upstream and downstream ends. The observers are set along the circle, centered at the jet exit center, with a radius of $100D_j$.

Figure 21 shows the 1/3 octave noise at observers angled at 30°, 60°, 90° and 120°. For all viewing azimuths, a significant noise reduction is observed in the WIW-treated nozzles. However, the noise increases slightly in the low-frequency band, especially in Case 1. The difference between the nozzles is mainly reflected in the low frequency band. In the part of $St \geq 1$, the noise attenuation trend of the WIW-treated nozzles is same. In the azimuths of 30° and 60°, the noise increases slightly in the low-frequency band. The effect of noise reduction in the 30° azimuth is not obvious. In the 90° azimuth, the noise in the low frequency band does not increase significantly. Case 2 has a good noise reduction effect at the entire frequency, and the noise reduces about 3.1 dB at the frequency of $St = 1.35$. In the upstream azimuth of 120°, Case 2 has a noise reduction effect in the low frequency band. However, Case 1 increases by about 1.5 dB in the range of $0.3 \leq St \leq 0.4$. In the middle and high frequency parts, the noise reduction effect of the WIW-treated nozzles is also weaker. Therefore, the noise reduction ability of Case 2 is better than Case 1.

The far-field directivity is shown in Fig. 22. By comparison with the baseline, solid evidences are achieved that the WIW-treated nozzles have the ability of noise suppression. Again, the noise reduction ability of Case 2 is better than Case 1. The noise reduction effect is weaker in the downstream and upstream directions, and the noise reduction

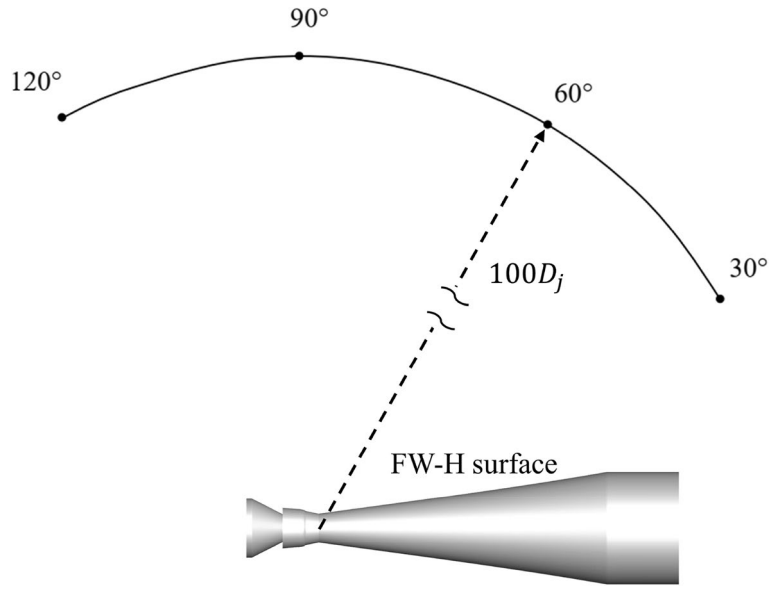

Fig. 20 Schematic view of the permeable FW-H source surface and definition of the far-field observers

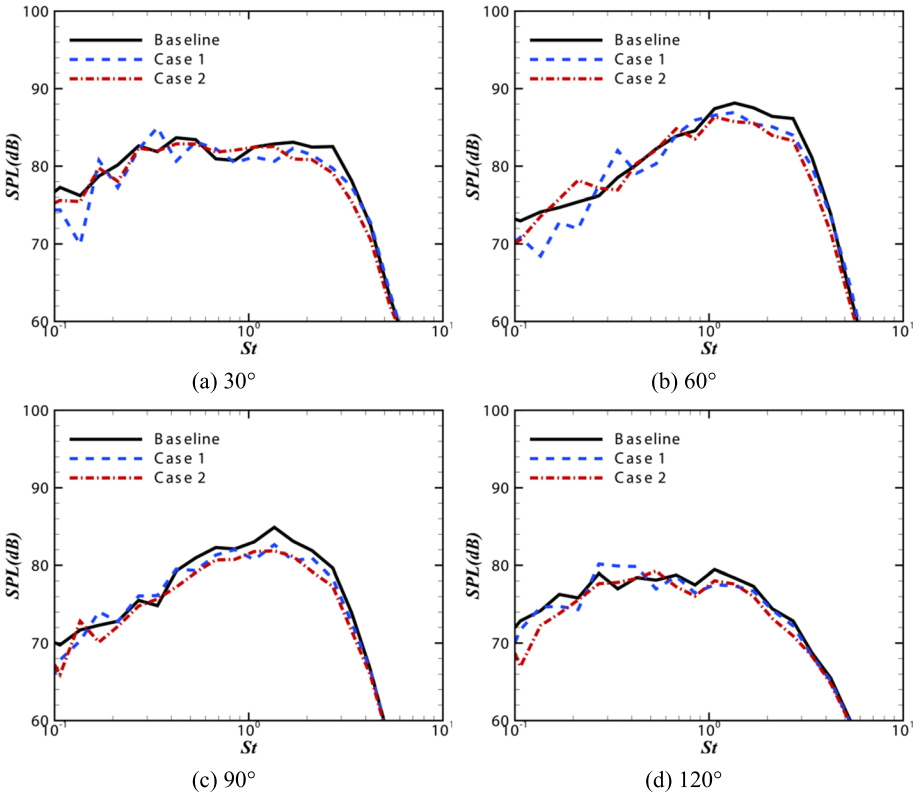

Fig. 21 Comparison of the 1/3 octave noise between the baseline and the WIW-treated nozzles. **a** 30°; **b** 60°; **c** 90°; **d** 120°

effect is best near the 90° direction. In order to further quantify the noise reduction effect, the OASPL difference between the WIW-treated nozzles and the baseline is presented in the form of a bar chart in Fig. 23. It can be seen from the bar chart that the

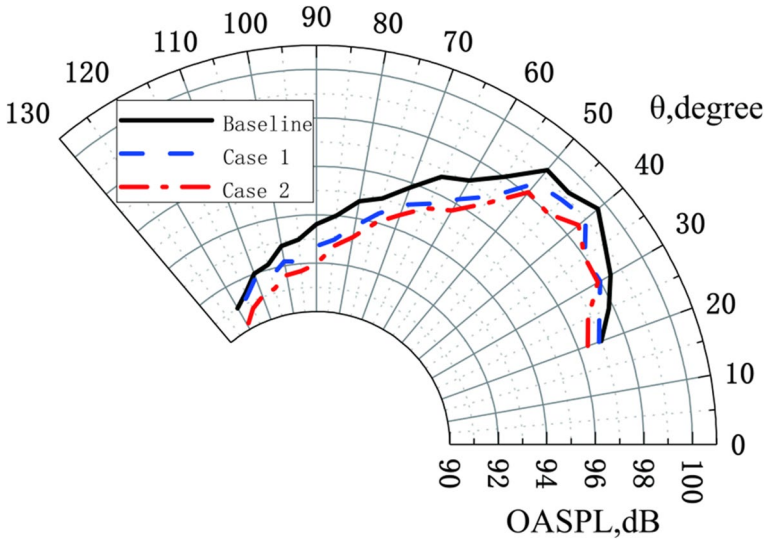

Fig. 22 Comparison of the OASPL directivity of the baseline and the WIW-treated nozzles at $r = 100D_j$

noise reduction effect of Case 1 is within 1 dB except for the 65° azimuth; especially in the upstream direction, the noise reduction effect is weak. The noise reduction effect of Case 2 nozzle exceeds 1 dB in the range of $40° - 100°$; especially in the azimuth of 90°, the OASPL is reduced by more than 1.6 dB. And Case 2 has a better noise reduction effect in both upstream and downstream directions.

The above discussions based on the turbulent flow structures, the near-field and the far-field noise have pointed to a solid conclusion that the WIW treatment is efficient in flow and noise control. The strongest noise suppression resides in the mid- to

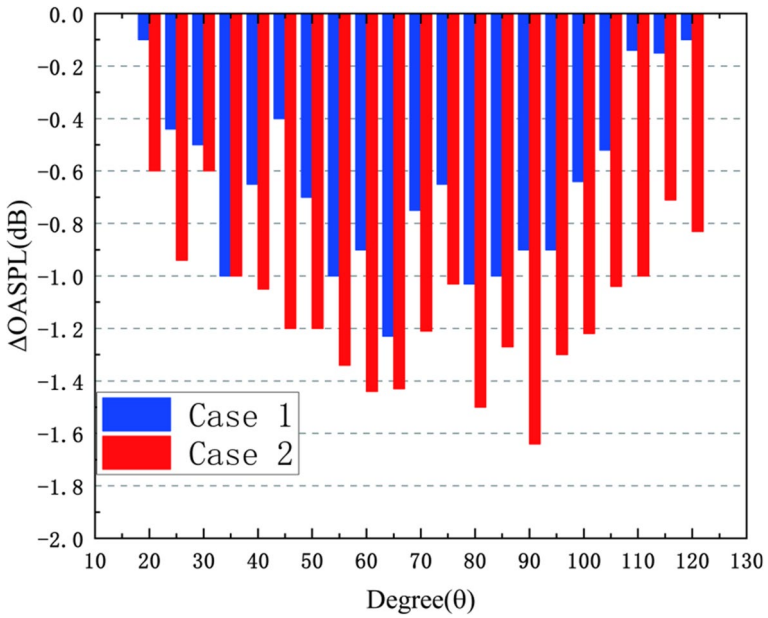

Fig. 23 Bar chart of OASPL difference between the WIW-treated nozzles and the baseline

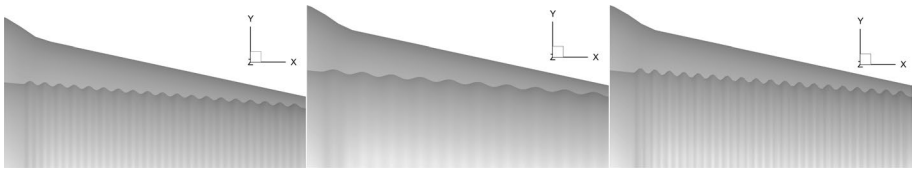

(a) Wave 1 (b) Wave 2 (c) Wave 3

Fig. 24 Model of the WIW-treated nozzles: **a** Wave 1 the reference; **b** Wave 2 with a larger wavelength; **c** Wave 3 with a larger wave amplitude (height)

high-frequency band. Large and long-paved wave pattern (Case 1) tends to increase the noise at low frequencies. Its ability in controlling the upstream- and downstream-radiated noise (dominated directions) is relatively weak. The small and short-paved wave pattern (Case 2) provides better noise reduction in all far-field directions with a small sacrifice at the low frequency. Therefore, the nozzle of Case 2 is selected as the basic wave pattern for further parametric studies.

4.3 Parametric studies of the WIW treatment

Parametric investigations were performed based on the nozzle of Case 2. Its WIW pattern is selected as the reference and labelled as Wave 1. Wave 2 and Wave 3 were created by changing the wavelength and the wave height, respectively. The resulted WIW-treated nozzles are shown in Fig. 24. The parameters are given in Table 6.

As shown in Fig. 25, the influence of wave parameters on the flow field is mainly reflected by the state of the shear layer at the nozzle exit. The introduction of the WIW treatment leads to intensified axial instability in the shear layer near the nozzle exit. As illustrated by the Q-isosurfaces, circumferential instability waves are introduced by the WIW treatment. This instability wave grows as the flow travels downstream, resulting in the breaking-down of the ring-shaped structures. Compared with the reference (Wave 1), the WIW pattern with larger wavelength (Wave 2) leads to an enhancement of the initial instability wave. As a result, the ring-shaped vortices break down almost instantly at the nozzle exit. The WIW pattern with larger amplitude (Wave 3) also leads to an enhancement of the initial instability wave, but the strength is much weaker.

As shown in Fig. 26, the far-field noise spectra are obtained by FW-H integration. The OASPL results in Section 4.2.2 show that the WIW-treated nozzles have better noise reduction at $40° - 100°$. Therefore, four far-field observers located at azimuths of 50°, 70°, 90° and 110° are selected for comparison. At all observers, all three WIW patterns show the ability of noise control. The most efficient noise reduction range remains the middle to high frequencies. The WIW patterns Wave 1 and Wave 3 show similar performance in noise suppression, while Wave 2 is the worst. For the low frequency noise, Wave 1 performs better than Wave 3.

The 1/3-octave spectra of these observers are given in Fig. 27. The acoustic performance of these nozzles becomes clearer. The Wave 3 has better noise reduction in the azimuth of 70°; however, it introduces extra noise in the low frequency band at 110°. Thus, a quick and simple assertion is that the WIW treatment is able to control jet noise; however, it's crucial to keep the wavelength and wave height in the suitable scales. The wavelength and wave amplitude of the WIW pattern should be small,

Table 6 Geometric parameters of different WIW patterns

Wave type	h/D_j	λ/D_j	h/λ
Wave 1	0.0064	0.05	0.128
Wave 2	0.0064	0.1	0.064
Wave 3	0.0096	0.05	0.192

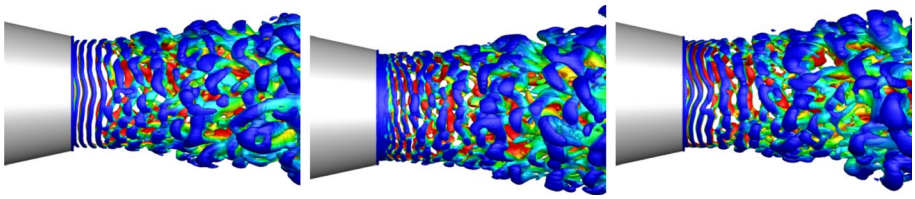

(a) Wave 1 (b) Wave 2 (c) Wave 3

Fig. 25 Iso-surface of $Q = 5\left(U_j^2/D_j\right)$: **a** Wave 1; **b** Wave 2; **c** Wave 3

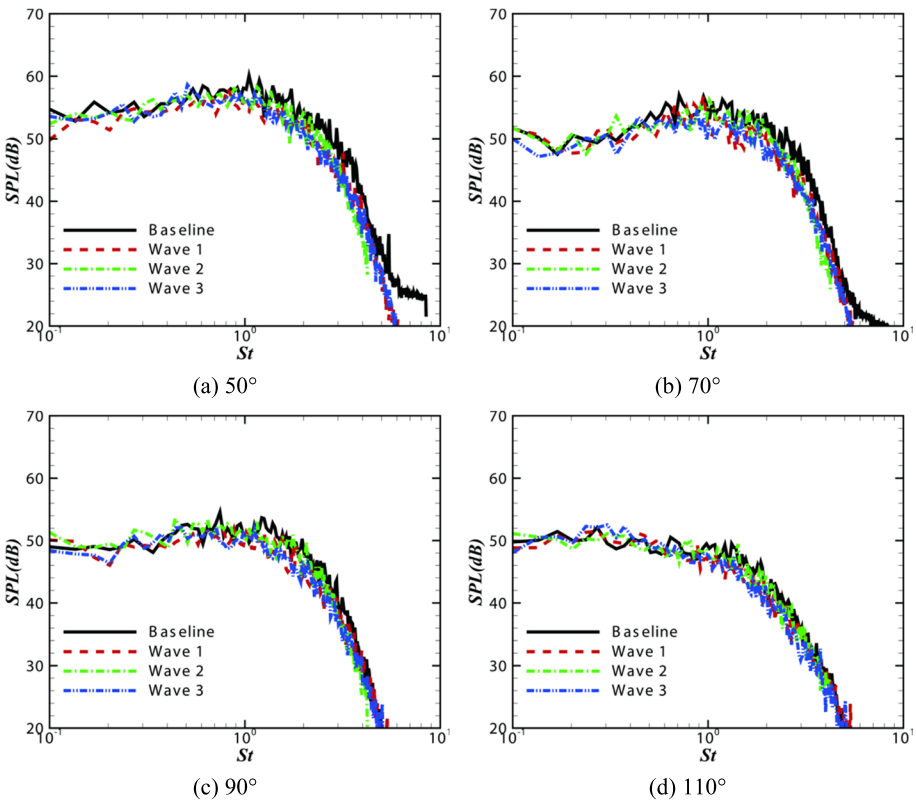

Fig. 26 Comparison of the noise spectra among the baseline and the WIW-treated nozzles. **a** 50°; **b** 70°; **c** 90°; **d** 110°

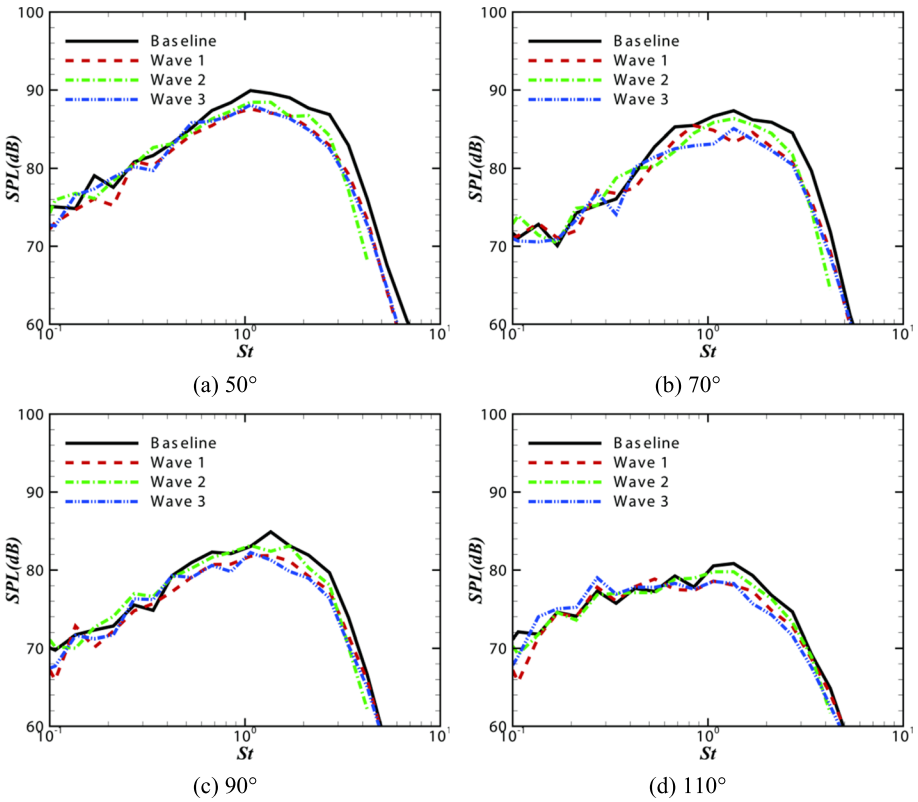

Fig. 27 Comparison of the 1/3 octave noise between the baseline and the WIW-treated nozzles. **a** 50°; **b** 70°; **c** 90°; **d** 110°

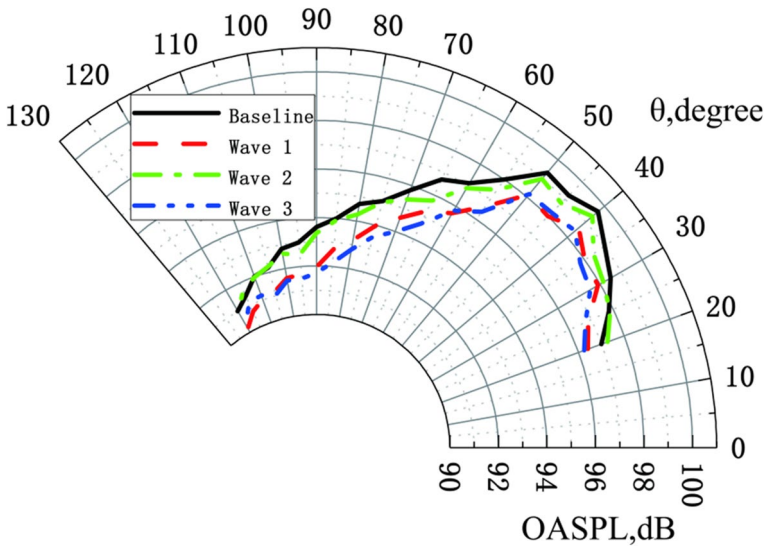

Fig. 28 Comparison of the OASPL directivity of the baseline and the WIW-treated nozzles at $r = 100D_j$

because the increase of the wavelength leads to the decrease in the amount of the overall noise control. And the increase of the wave amplitude tends to increase the low-frequency noise.

The far-field directivity is shown in Fig. 28. Compared with the baseline, once again, evidences are achieved that the WIW-treated nozzles have the ability of noise suppression. The noise reduction ability of Wave 2 is weaker than Wave 1 and Wave 3. The noise reduction effect is weaker in the downstream and upstream directions, and the noise reduction effect is best in the azimuths of $40° - 100°$. In order to further quantify the noise reduction effect, the OASPL difference between the WIW-treated nozzles and the baseline is presented in the form of a bar chart in Fig. 29. The bar chart shows that the noise reduction effect of Wave 2 is within 0.5 dB; especially in the upstream direction, the noise increases at 20°. The noise reduction effect of Wave 3 exceeds 1.5 dB in the range of $70° - 90°$; especially in the azimuth of 90°, the OASPL is reduced by more than 1.9 dB. Therefore, Wave 3 has the best noise reduction among the three WIW-treated nozzles.

The prerequisite of noise control techniques is the maintenance of the aerodynamic performance, for instance, the thrust for a jet. The thrust loss of the WIW-treated nozzles is calculated by surface integral of the mean pressure at the nozzle exit section. The specific calculation results are given in Table 7. It can be seen from the data in Table 7 that the impact of the wavy inner wall on the thrust is small. For Wave 3 with the best noise reduction ability, only 1.09% of the thrust is lost. Interestingly, while the noise reduction of Wave 2 is weak, its thrust increases by 4.81%. It can be seen that the use of the WIW-treated nozzles can ensure the thrust of the engine and at the same time have

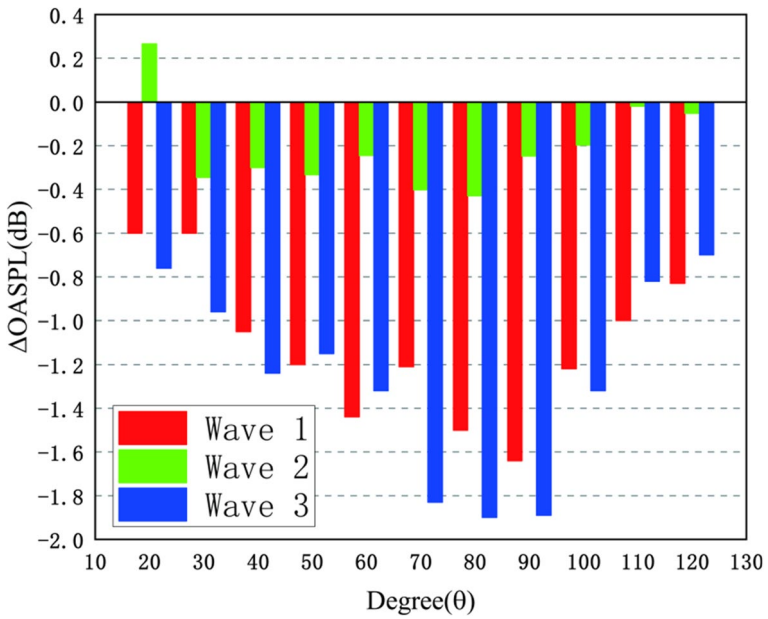

Fig. 29 Bar chart of OASPL difference between the WIW-treated nozzles and the baseline

Table 7 Thrust of nozzles

Nozzle	Baseline	Wave 1	Wave 2	Wave 3
Thrust	219.17 N	213.97 N	229.73 N	216.78 N

a good control effect on the jet noise. Therefore, the WIW treatment technology has a real application in jet noise control.

4.4 Noise control mechanism of the WIW treatment

The flow properties near the nozzle exit are discussed to understand the noise control mechanisms of the WIW treatment technique. The initial shear layer disturbances, radial and azimuthal autocorrelation functions, distributions of the pressure time gradient, the turbulent kinetic energy and the acoustic source from the TA model are analyzed. The nozzle treated by Wave 3 is compared with the baseline.

4.4.1 The initial shear layer disturbances

Figure 30 shows the initial shear layer at the nozzle exit described by the Q-criteria iso-surfaces. The evolution of the vortex rings indicates the development of the shear-induced Kelvin–Helmholtz instability. For the baseline nozzle, the vortex rings are almost uniform near the nozzle exit before the breaking-down of vortex rings at about $x/D_j = 1.0$. Strong circumferential instability waves, which form in the jet pipe by the WIW treatment, are introduced to the initial vortex rings. Measured from Fig. 30, the amplitude of such instability waves is about $a_i = 0.083D_j$, with wavelength of about $\lambda_i = \pi D_j/3$. These initial waves enhance the interaction between the shear layer and the ambient flow and, thus, accelerate the development of the shear-layer instability and fragmentation. This effect is similar to that of the chevron nozzles, but the interference is much gentler. So, the enhancement of jet mixing is also a key mechanism of the noise control from the WIW treatment. In order to achieve the details of the WIW-induced initial disturbances, the azimuthal distribution of the magnitude of vorticity at $x/D_j = 0.5$, $r/D_j = 0.5$ (axial position as shown in Fig. 30) is extracted and plotted in Fig. 31.

As shown in Fig. 31a, the vorticity magnitude (normalized by U_j/D_j) remains relatively stable around the ring-shaped vortex. The sub-figure shows the vorticity magnitude transformed to the wavenumber domain. The shear-layer instability wave is dominated by the component with a wavenumber $k \approx 4$, for the baseline nozzle. This component is the inherent instability mode of the SMC000 nozzle. By WIW-treating with pattern

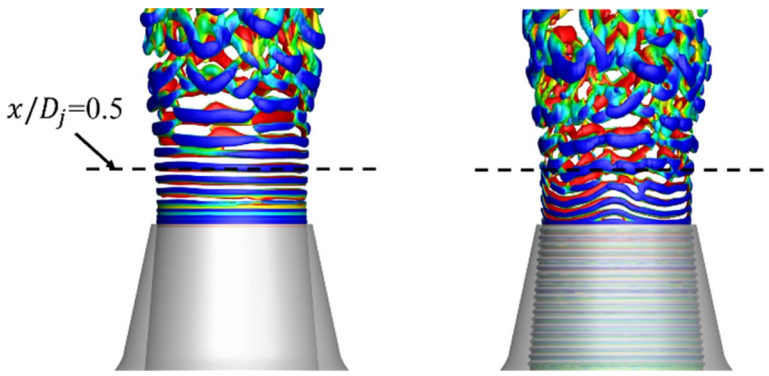

Fig. 30 Iso-surface of $Q = 5\left(U_j^2/D_j\right)$: **a** Baseline; **b** Wave 3

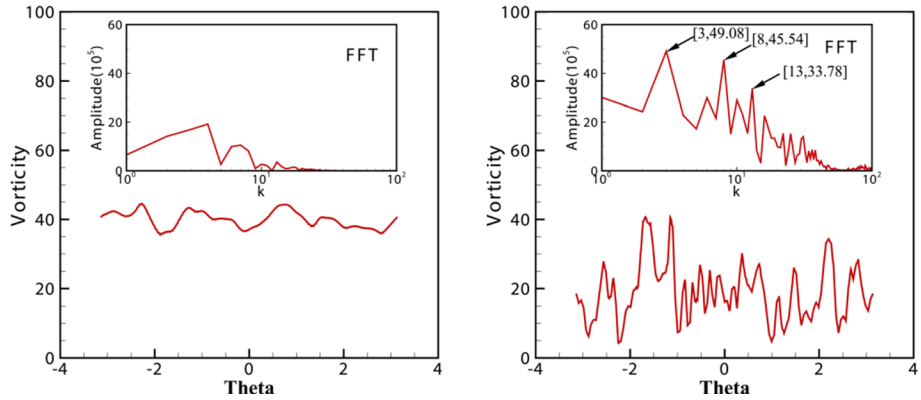

Fig. 31 Azimuthal distribution of the magnitude of vorticity at $x/D_j = 0.5, r/D_j = 0.5$, and corresponding spectrum in the wavenumber domain: **a** Baseline; **b** Wave 3

Wave 3, as shown in Fig. 31b, the azimuthal distribution of the vorticity magnitude is significantly disturbed. Three extra instability modes are introduced with wavenumbers $k \approx 3$, $k \approx 8$, and $k \approx 13$. These extra modes are superposed on the inherent mode at $k \approx 4$, resulting in a complex vorticity distribution along the vortex rings. As a result, the breaking-down of the vortex rings is greatly advanced.

4.4.2 Distribution of the turbulent kinetic energy

Figure 32 shows the turbulent kinetic energy (TKE) of the baseline and Wave 3, where the turbulent kinetic energy k is expressed as $k = \frac{1}{2}\left(u'^2 + v'^2 + \omega'^2\right)$, where u', v' and ω' are the velocity fluctuation in x, y and z directions, respectively. The WIW treatment is able to control the peak turbulent kinetic energy along the shear layer. The peak turbulent kinetic energy of the baseline is 3986.4 m^2/s^2 and that of Wave 3 is 3335.6 m^2/s^2, a decrease of nearly 16.3%. The turbulent kinetic energy is an important parameter for turbulent mixing noise. The reduction of the turbulent kinetic energy is another reason to explain the noise suppression ability of the WIW treatment technique.

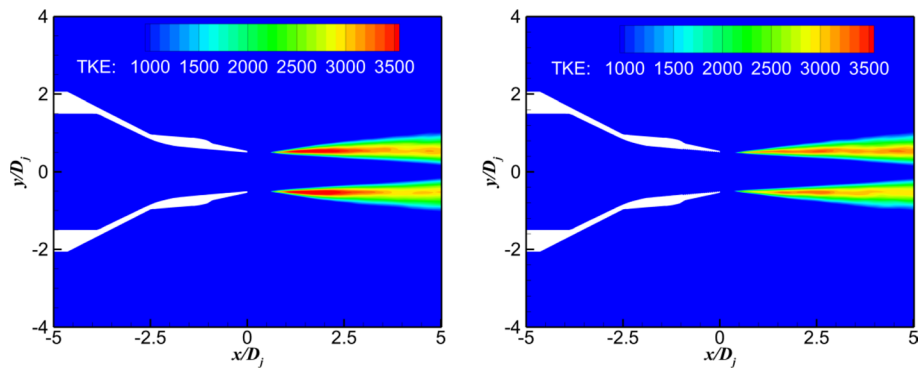

Fig. 32 Distributions of the turbulent kinetic energy: **a** Baseline; **b** Wave 3

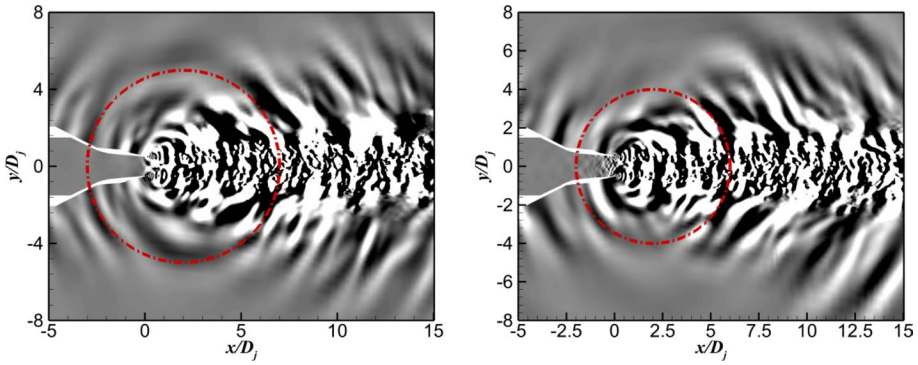

Fig. 33 Pressure time gradient: **a** Baseline; **b** Wave 3. The greyscale ranges from -10^6 to 10^6 Pa · s^{-1}

4.4.3 Distribution of the pressure time gradient

Figure 33 shows the use of pressure time gradient to describe the propagation process of acoustic waves from the near- to far-field. Compared to the baseline, Wave 3 has a more complex sound radiation process near the nozzle exit. Dashed-red circles are placed at a radius with similarly strong pressure footprints for both cases. By comparing the size of these circles and the enclosed region, it can be observed that the sound pressure footprints generated by nozzle Wave 3 are much weaker than those of the baseline. This indicates that the WIW treatment is effective in reducing the generation and radiation of jet noise. This effect is particularly strong in the direction of 70° – 90°, which is where the strongest noise suppression is achieved in the far-field.

4.4.4 The noise source term of the TA model for fine-scale turbulence

The TA model proposed by Tam and Auriault [38] is classical for the prediction and analysis of fine-scale-turbulence induced jet noise. They defined the acoustic source based on the two-point spatio–temporal correlation function. Treated by a Gaussian modeling method, the noise source space–time correlation function is expressed as

$$\langle \frac{dq_s(x_1 \cdot t_1)}{dt_1} \frac{dq_s(x_2 \cdot t_2)}{dt_2} \rangle = \frac{\widehat{q}_s^2}{c^2 \tau_s^2} \times exp\left\{ -\frac{|\xi|}{\overline{u}\tau_s} - \frac{ln2}{l_s^2}\left[(\xi - \overline{u}\tau)^2 + \eta^2 + \zeta^2 \right] \right\}, \tag{19}$$

where $\xi = x_1 - x_2$, $\eta = y_1 - y_2$, $\zeta = z_1 - z_2$, $\tau = t_1 - t_2$. c is a constant, and $\widehat{q}_s^2$, l_s and τ_s are three parameters in the acoustic source model. $\widehat{q}_s^2$ is the small-scale turbulent kinetic energy per unit volume, l_s the characteristic length, and τ_s the characteristic dissipation time of small-scale turbulence. These variables are linked to the TKE and the dissipation rate by the following relations:

$$\begin{cases} \widehat{q}_s^2/c^2 = A^2 q^2, q = \frac{2}{3}\rho k, \\ l_s = c_l\left(k^{\frac{3}{2}}/\varepsilon\right), \tau_s = c_\tau\left(\frac{k}{\varepsilon}\right), \end{cases} \tag{20}$$

where q is proportional to the TKE that we have discussed above. A, c_l and c_τ are three empirical constants. The coefficient c is expected to be less than 1.0 if the assumption is satisfied that flow fluctuating time is shorter than the turbulence decay time. Based on

the TA model, $\widehat{q}_s^2/c^2$, l_s and τ_s are three critical parameters related to jet noise. The first parameter $\widehat{q}_s^2/c^2$ is positively related to the source intensity, while, l_s and τ_s are negatively related to the source intensity. Thus, they can be applied to help unveil the noise control mechanism of the WIW-treated nozzles. The main difference introduced by the WIW treatment is the acceleration of the shear-layer instability that happens near the nozzle lip-line. Figure 34 compares the values of $\widehat{q}_s^2/c^2$, l_s, τ_s and their combination function C_s in the shear-region between the baseline and the WIW-treated nozzle. The combination function C_s is defined as

$$C_s = \frac{\widehat{q}_s^2}{c^2\tau_s^2} \times exp\left\{-\frac{r_s}{\overline{u}\tau_s} - \frac{{r_s}^2}{l_s^2}\right\}, \tag{21}$$

where $\overline{u}$ is the mean axial jet velocity. By assuming that the term $|\xi|^2$ and $(\xi - \overline{u}\tau)^2 + \eta^2 + \zeta^2$ have the same order of magnitude, an arbitray constant, r_s, is applied to scale the value of C_s. The value we take for r_s is 0.01 for current cases. Thus, C_s represents the overall effect of $\widehat{q}_s^2/c^2$, l_s and τ_s. As shown in Fig. 34a, compared with the baseline nozzle, $\widehat{q}_s^2/c^2$ observed in case Wave 3 is slightly larger in the range of $x/D_j \in [0, 5.7]$. After reaching $x/D_j = 5.7$, a significant reduction is observed in the WIW-treated nozzle. The position, $x/D_j = 5.7$, is close to the end of the potential core. So, the WIW treatment leads to an enhancement of the TKE before the jet reaches the end of the potential

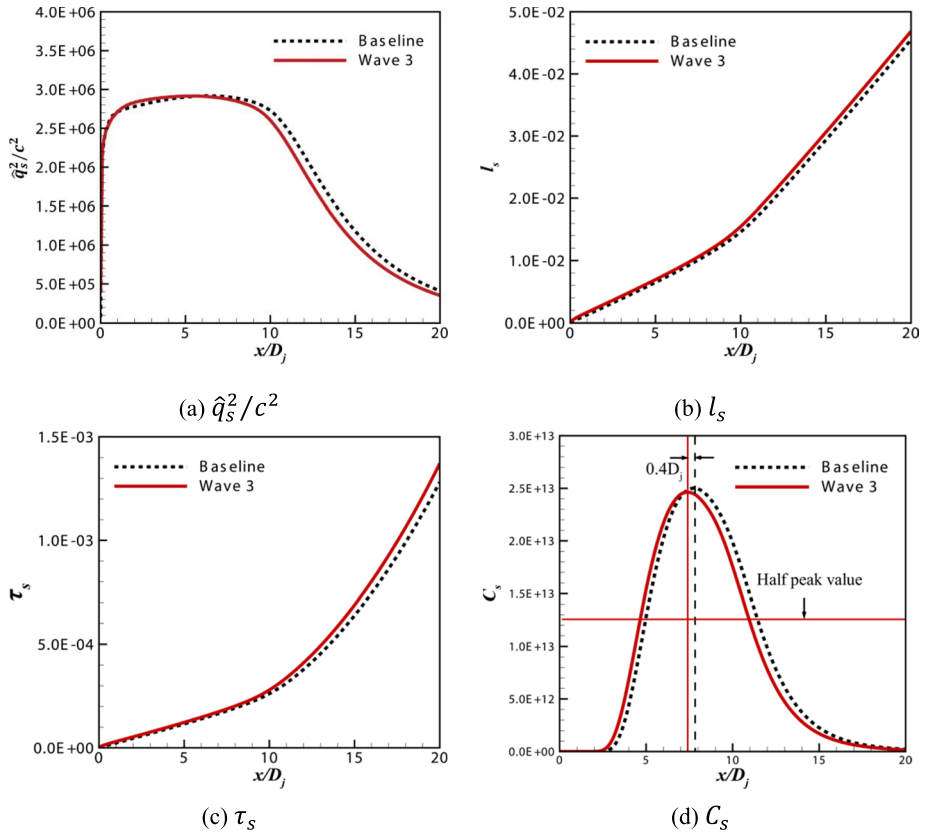

Fig. 34 Comparison of TA acoustic source parameters: **a** $\widehat{q}_s^2/c^2$; **b** l_s; **c** τ_s; **d** C_s. Referred to Ref. [38], the empirical parameters are set to be $c_l = 0.256$, $c_\tau = 0.233$, $A = 0.755$ and $c = 0.5$

core. While after the potential core, the TKE decays much faster. The overall effect points to the control of the source of jet noise. Figure 34b-c shows the distributions of l_s and τ_s. The WIW treatment leads to solid increases in the turbulence characteristic length and the characteristic dissipation time of small-scale turbulence. As a result, the jet noise source from the fine-scale turbulence is suppressed. The overall effect of the WIW treatment on the source of fine-scale turbulence noise is plotted in Fig. 34d. A stronger superposition effect of source attenuation is observed. The peak source position is moving close to the nozzle exit by $0.4D_j$. Measured from the C_s plotting, the axial length of the source zone (measured at half amplitude of C_s) is reduced by 1.57%, and the integral of C_s along x is reduced by 3.16%. Thus, it is explained that the WIW treatment has the ability of reducing the fine-scale noise source of jet flow, which is the main sound source of high-frequency noise. This also explains that the noise reduction is more significant in the middle to high frequency.

5 Conclusions

A passive control technique called the WIW treatment has been proposed to reduce the exhaust noise of jet engines. This technique involves treating the inner wall of the engine nozzle with wavy patterns. The classical SMC000 nozzle was selected to evaluate the ability of noise suppression and the underlying noise control mechanisms. A detailed analysis of high subsonic cold ($Ma = 0.9$, $T_j/T_\infty = 0.835$) jet flows with and without WIW treatment was carried out.

The WIW treatment applied to the SMC000 nozzle results in a reduction of up to 1.9 dB in OASPL without compromising jet thrust. Furthermore, the WIW-treated nozzles are more effective at suppressing mid- to high-frequency broadband noise, with the direction range of $40^\circ - 100^\circ$ benefiting the most. Parametric studies indicate that the noise attenuation ability of the WIW treatment is sensitive to the wave patterns, and for optimal noise control, the wavelength and wave amplitude of the WIW pattern should be small. Increasing the wavelength tends to weaken the overall noise control, and increasing the wave amplitude may generate additional low-frequency noise.

The noise control mechanism of the WIW-treated nozzles is attributed to the enhancement of jet mixing. The WIW treatment introduces several extra initial instability modes, which are superposed with the inherent instability modes of the baseline nozzle to accelerate the breaking-down of vortex rings near the jet exit. This results in jet flows that are much closer to isotropic turbulence, and compared to the baseline, the peak value of the TKE in the jet shear-layer is decreased by up to 16.3%. As a result, the location, strength, and scale of the jet noise source are modified. Visualizing the generation and evolution of jet noise using the pressure time gradient shows that this noise control technique is particularly efficient in the direction of $70^\circ - 90^\circ$. By examining the noise source from the Tam-Auriault fine-scale turbulence noise model, it is found that the WIW treatment is effective in controlling all three key factors: the scaled TKE ($\widehat{q}_s^2/c^2$), the characteristic length (l_s), and the characteristic dissipation time (τ_s) of jet turbulence. This explains the ability of the WIW treatment to suppress mid- to high-frequency broadband noise.

Acknowledgements
Not applicable.

Authors' contributions
Prof. Xiaoquan Yang conceptualized the article. Huyue Mao drafted the manuscript and conducted the numerical simulations. Dr. Xiaolong Tang played a leading role in analyzing and revising the manuscript. Prof. Jue Ding and Prof. Peifen Weng supervised this study. The authors read and approved the final manuscript.

Funding
This work is supported by grants from the National Natural Science Foundation of China (No. 11702329, No. 12102247), the National Science and Technology Major Project (J2019-II-0013–0033) and the Shanghai Key Lab of Vehicle Aerodynamics and Vehicle Thermal Management Systems (No. VATLAB-2021–01).

Availability of data and materials
The data that support the findings of this study are available from the corresponding author upon reasonable request.

Declarations

Competing interests
The authors declare no competing interests.

Received: 26 February 2023 Accepted: 6 April 2023
Published online: 09 May 2023

References

1. Wickenheiser TJ, Sehra AK, Seng GT et al (2003) Emissionless aircraft: requirements and challenges. In: AIAA international air and space symposium and exposition: the next 100 years, Dayton, 14–17 July 2003
2. Sheng ZQ, Liu JY, Yao Y et al (2020) Mechanisms of lobed jet mixing: about circularly alternating-lobe mixers. Aerosp Sci Technol 98:105660
3. Bridges J, Brown CA (2004) Parametric testing of chevrons on single flow hot jets. In: The 10th AIAA/CEAS aeroacoustics conference, Manchester, 10–12 May 2004
4. Greska B, Krothapalli A, Seiner JM et al (2005) The effects of microjet injection on an F404 jet engine. In: The 11th AIAA/CEAS aeroacoustics conference, Monterey, 23–25 May 2005
5. Kumar PA, Kumar S, Mitra AS et al (2018) Fluidic injectors for supersonic jet control. Phys Fluids 30(12):126101
6. Karon AZ, Ahuja KK (2013) Effect of nozzle-exit boundary layer on jet noise. In: The 51st AIAA aerospace sciences meeting including the new horizons forum and aerospace exposition, Grapevine, 7–10 January 2013
7. Bradbury LJS, Khadem AH (1975) The distortion of a jet by tabs. J Fluid Mech 70(4):801–813
8. Xu CY, Chen LW, Lu XY (2010) Large-eddy simulation of the compressible flow past a wavy cylinder. J Fluid Mech 665:238–273
9. Xu CY, Hou B, Wang Z et al (2020) Effect of Mach number on the compressible flow past a wavy-axis cylinder. Aerosp Sci Technol 104:105943
10. Choi HS, Suzuki K (2005) Large eddy simulation of turbulent flow and heat transfer in a channel with one wavy wall. Int J Heat Fluid Flow 26(5):681–694
11. Bechert DW, Bruse M, Hage W et al (1997) Experiments on drag-reducing surfaces and their optimization with an adjustable geometry. J Fluid Mech 338:59–87
12. Meng K, Zhang H, Shi Y et al (2011) Numerical study for turbulent flow of drag and flow noise with wavy wall. J Shanghai Jiaotong Univ (Sci) 16:45–54
13. Liu XW, Hu ZW, Thompson DJ et al (2018) Reduction of aerodynamic noise from square bars by introducing spanwise waviness. J Sound Vib 435:323–349
14. Chen G, Tang X, Yang X et al (2021) Noise control for high-lift devices by slat wall treatment. Aerosp Sci Technol 115:106820
15. Chen B, Yang X, Chen G et al (2022) Numerical study on the flow and noise control mechanism of wavy cylinder. Phys Fluids 34(3):036108
16. Liu Q, Lai H (2021) Coherent structures in a compressible turbulent plane jet. Phys Fluids 33(10):105109
17. Sheng J, Li X, Wang Y et al (2022) Screech in transient supersonic jets. Phys Fluids 34(9):096102
18. Es-Sahli O, Sescu A, Afsar MZ et al (2020) Investigation of wakes generated by fractal plates in the compressible flow regime using large-eddy simulations. Phys Fluids 32(10):105106
19. Zhu M, Arroyo CP, Pouangué AF et al (2018) Isothermal and heated subsonic jet noise using large eddy simulations on unstructured grids. Comput Fluids 171:166–192
20. Ffowcs Williams JE, Hawkings DL (1969) Sound generation by turbulence and surfaces in arbitrary motion. Philos Trans R Soc Lond A 264(1151):321–342
21. Biancherin A, Lupoglazoff N, Rahier G et al (2002) Comprehensive 3D unsteady simulations of subsonic and supersonic hot jet flow-fields: Part 2: acoustic analysis. In: The 8th AIAA/CEAS aeroacoustics conference & exhibit, Breckenridge, 17–19 June 2002
22. Uzun A, Lyrintzis AS, Blaisdell GA (2004) Coupling of integral acoustics methods with LES for jet noise prediction. Int J Aeroacoust 3(4):297–346
23. Mendez S, Shoeybi M, Lele SK et al (2013) On the use of the Ffowcs Williams-Hawkings equation to predict far-field jet noise from large-eddy simulations. Int J Aeroacoust 12(1–2):1–20

24. Zhang Y, Xiao Y, Liu R et al (2022) Aeroacoustic prediction based on large-eddy simulation and the Ffowcs Williams-Hawkings equation. Adv Aerodyn 4(1):19
25. Shur ML, Spalart PR, Strelets MKh (2005) Noise prediction for increasingly complex jets. Part II: applications. Int J Aeroacoust 4(3):247–266
26. Vreman AW (1995) Direct and large-eddy simulation of the compressible turbulent mixing layer. Dissertation, University of Twente
27. Lenormand E, Sagaut P, Ta Phuoc L et al (2000) Subgrid-scale models for large-eddy simulations of compressible wall bounded flows. AIAA J 38(8):1340–1350
28. Farassat F (2007) Derivation of Formulations 1 and 1A of Farassat. NASA Tech memo NASA/TM-2007-214853
29. Casalino D (2003) An advanced time approach for acoustic analogy predictions. J Sound Vib 261(4):583–612
30. Bridges J, Wernet MP (2011) The NASA subsonic jet particle image velocimetry (PIV) dataset. NASA Tech Memo NASA/TM-2011-216807
31. Tanna HK (1997) An experimental study of jet noise part I: turbulent mixing noise. J Sound Vib 50(3):405–428
32. Housman JA, Stich GD, Kiris CC (2017) Jet noise prediction using hybrid RANS/LES with structured overset grids. In: The 23rd AIAA/CEAS aeroacoustics conference, Denver, 5–9 June 2017
33. Van Albada GD, van Leer B, Roberts WW Jr (1982) A comparative study of computational methods in cosmic gas dynamics. Astron Astrophys 108(1):76–84
34. Pulliam TH (1993) Time accuracy and the use of implicit methods. In: The 11th computational fluiddynamics conference, Orlando, 6–9 July 1993
35. Dailey LD, Pletcher RH (1996) Evaluation of multigrid acceleration for preconditioned time-accurate Navier-Stokes algorithms. Comput Fluids 25(8):791–811
36. Xia H (2015) Turbulent jet characteristics for axisymmetric and serrated nozzles. Comput Fluids 110:189–197
37. Angelino M, Xia H, Page GJ (2020) Influence of grid resolution on the spectral characteristics of noise radiated from turbulent jets: sound pressure fields and their decomposition. Comput Fluids 196:104343
38. Tam CKW, Auriault L (1999) Jet mixing noise from fine-scale turbulence. AIAA J 37(2):145–153

Publisher's Note